High-Speed Spectral-Domain Optical Coherence Tomography and *In Vivo* Human Eye Imaging

Shuichi Makita
(Doctoral Program in *Applied Physics*)

Submitted to the Graduate School of

Pure and Applied Sciences

in Partial Fulfillment of the Requirements

for the Degree of Doctor of Philosophy in
Engineering

at the
University of Tsukuba

To my mother and brother, for their support and patience ...

Abstract

Spectral-domain optical coherence tomography (SD-OCT) is a cross-sectional imaging technique for biological tissues with high spatial resolutions. Owing to the superior sensitivity of SD-OCT over the conventional time-domain OCT (TD-OCT), it has undergone rapid development in the past few years and has proved to be a promising technique for clinical and biological applications. One limitation of SD-OCT is the formation of coherent ghost images, which restrict the imaging depth range. In order to overcome this problem, one solution that does not sacrifice the high imaging speed is presented. The basics of the procedure are described and altered so as to suit high-speed imaging and *in vivo* biological tissue imaging has been demonstrated.

The most successful application of OCT technology is in retinal disease diagnosis. The high sensitivity of SD-OCT is suitable for this application since the level of light illumination is restricted for reasons of eye safety. High-speed *in vivo* retinal imaging is achieved. Three-dimensional (3D) imaging is achived with motion correction, although the involuntary head movements are problematic. Two types of motion correction methods are introduced for inter-axial-scan and inter-frame motion, respectively. After the corrections, the 3D structures of a healthy human retina and retinal diseases (age-related macular degeneration and macular hole) are observed.

Finally, noninvasive angiography for *in vivo* human eye is demonstrated. Three-dimensional flow imaging has been performed with SD-OCT and the 3D vasculature of ocular vessels has been visualized. By integrating the volume sets of flow images, two-dimensional (2D) images of blood vessels are obtained. Retinal and choroidal blood vessel images are simultaneously produced by separating the volume set into a retinal part and a choroidal part. These images are compared to the existing techniques of ophthalmic angiography, i.e., fluorescein angiography and indocyanine green angiography.

Acknowledgments

I would like to thank my supervisor, Professor Toyohiko Yatagai. Without his encouragement, enthusiastic support and guidance, this work would have not been possible.

I have been fortunate enough to research in Computational Optics Group. Doctor Yoshiaki Yasuno has been a good adviser and mentor since the beginning of this research. He provide motivated and enthusiastic atmosphere with many critical discussions. I would like to acknowledge the great contributions of many colleagues and ex-colleagues in COG. The meaningful discussions and insights of Masahiro Yamanari and Youngjoo Hong, the hard works of Yoshifumi Nakamura and Gouki Aoki are indispensable in this research.

I also have to mention about a great contribution of Dr. Masahiro Miura from Tokyou Medical University. Retinal disease imaging could not have been done without his help and contributions of patients who are diagnosed by him.

This research could not be accomplished without the support from Japan Society for the Promotion of Science (Research Fellowships for Young Scientists).

In the last, I really thanks to my family for making me aside from research works.

Table of Contents

Abstract **i**

Acknowledgments **iii**

Table of Contents **v**

List of Figures **vii**

Acronym **xi**

1 Introduction **1**
1.1 Overview 1
1.2 Spectral-domain optical coherence tomography 1
1.2.1 Resolutions 3
1.2.2 Sensitivity advantage 3
1.2.3 Axial range limitations 5
1.3 Aim of thesis 5

2 High-speed complex SD-OCT **7**
2.1 Overview of complex SD-OCT 8
2.2 Simultaneous BM-mode scanning 10
2.3 High-speed BM-mode scanning 12
2.4 Discussion 13
2.5 Summary 14

3 Retinal imaging by SD-OCT **15**
3.1 Ophthalmic high-speed SD-OCT 15
3.2 Ultrahigh-resolution SD-OCT 17
3.2.1 Numerical dispersion compensation 20
3.3 Motion correction 21
3.3.1 Axial motion correction by Doppler shift 22
3.3.2 Correction by cross-correlation between neighboring frames 22
3.3.3 Performance of axial shift correction 23
3.4 Fast fundus preview 26

3.5 Retinal imaging 27
3.5.1 Imaging of retinal diseases 28
3.5.2 Discussions 29
3.6 Summary 29

4 Optical coherence angiography **33**
4.1 Blood flow imaging by SD-OCT 34
4.1.1 Elimination of motion artifacts 35
4.2 OCA for the human eye 39
4.3 Results 40
4.3.1 Three-dimensional vasculature imaging 40
4.3.2 *En face* vasculature imaging 43
4.4 Summary 50

5 Conclusion **51**

A Signal-to-noise ratio of SD-OCT **53**

B Calibration of the spectrometer **57**

References **59**

List of Figures

1.1 Schematic diagram of SD-OCT 2

2.1 Optical scheme of a complex SD-OCT. CL: collimator lens, Ls: lenses, Obj.: objective lens, BS: beam splitter, PS: pupil stop, and PZT: piezoelectric transducer. The broadband light source is an SLD with a 828 nm central wavelength and a 40 nm band width. The CCD camera is a line-scan CCD camera with 2048 pixels. . . 8
2.2 Time charts of B-scans and M-scans for (i) a conventional phase-shifting SD-OCT, (ii) a BM-scan SD-OCT and, (iii) the modified BM-scan SD-OCT. 9
2.3 A flow diagram of the phase reconstruction procedure of a BM-scan SD-OCT. 10
2.4 (i) Non-complex SD-OCT image, and (ii) the complex BM-scan SD-OCT image of a plastic plate with a covering layer. 11
2.5 (i) Conventional non-complex, (ii) interlaced full-range, and (iii) full-range SD-OCT images of an *in vivo* sweat duct in a human finger pad taken with an acquisition time of 27 ms. 12

3.1 Schematic of a high-speed spectral-domain OCT system 16
3.2 Depth-dependent signal-to-noise ratio decay of the ophthalmic SD-OCT system. 17
3.3 SD-OCT image of the human retina *in vivo*. Several retinal structures appear. RNFL: retinal nerve fiber layer, GCL: ganglion cell layer, IPL: inner plexiform layer, INL: inner nuclear layer, OPL: outer plexiform layer, ONL: outer nuclear layer, ELM: external limiting membrane, IS/OS: inner/outer segments junction, RPE: retinal pigment epithelium, CC: choriocapillaris. The image size is 5.6 mm $\times$ 1 mm (lateral $\times$ depth). 18
3.4 Depth-dependent signal-to-noise ratio decay of the UHR-SD-OCT system. 19
3.5 Depth dependence of axial resolution in the UHR-SD-OCT system 19
3.6 Cost function for dispersion compensation. (a) Second-order coefficient, (b) third-order coefficient. 20

3.7 Ultrahigh-resolution retinal cross-section (a) with and (b) without dispersion compensation. 21
3.8 A sequence of OCT images and flow images of the human eye. Each image comprises 4000 axial scans and has a size of 5 mm $\times$ 1 mm (lateral $\times$ depth). The OCT images (A) without and (B) with the motion correction for adjacent axial scans are shown. The black arrow denotes the region in which axial image distortion has occurred. (C) Bi-directional flow and (D) the power of Doppler shift images show some vessels. Two retinal blood vessels appear in the bi-directional flow image (white circle). In the power of the Doppler shift image, the retinal vessels (upper white circle) and some choroidal vessels (two lower white circles) appear. Multimedia file is available on http://www.opticsexpress.org/abstract.cfm?id=97672 24
3.9 Comparison of the cross section of the 3D OCT volume along the slow-scanning direction. The fundus projection image (A) is produced from the 3D OCT volume set. White arrows represent the fast-scanning direction. The cross-sectional images (B) without motion correction, (C) with correction of the axial shift between neighboring frames, and (D) with correction of the axial shift between adjacent axial scans and neighboring frames corresponding to the red line in (A). 25
3.10 Fundus images of the human macula produced by (A) the preview mode and (B) integrating OCT signals. The imaging area size is 2.7 $\times$ 2.7 mm^2. 26
3.11 Fundus images of the ONH produced by (A) the preview mode and (B) integrating OCT signals. The imaging area is 2.7 $\times$ 2.7 mm^2. . 27
3.12 Three-dimensional image of the macula. (a) Fundus image created from 3D OCT volume set, (b) volume rendered image of 3D OCT image. S: superior, I: inferior, N: nasal, T: temporal. The imaging area size is 2.7 $\times$ 2.7 mm^2 (horizontal $\times$ vertical, 250 $\times$ 250 axial scans). The total imaging time for one volume set is 3.5 s. 28
3.13 Three-dimensional image of the ONH. (a) Fundus image created from 3D OCT volume set, (b) volume rendered image of 3D OCT image. S:, superior, I: inferior, N: nasal, T: temporal. The imaging area size is 2.7 $\times$ 2.7 mm^2 (horizontal $\times$ vertical, 250 $\times$ 250 axial scans). The total imaging time for one volume set is 3.5 s. 29
3.14 Three-dimensional imaging result for age-related macular degeneration (74-year-old Asian male, left eye). The imaging area size is 2.5 $\times$ 2.5 mm^2 (512 $\times$ 128) axial scans. (a) Fundus image created from the OCT volume set. (b),(c),(d) Cross-sectional images corresponding to the white lines in (a). In (b), the white arrow indicates RPE detachment. In (c), some macular cysts are shown (white arrows). 30

3.15 High definitive cross-section of a macular hole (70-year old Asian male, left eye). The imaging range is 2 mm × 5 mm (lateral × axial). The image consists of 2000 axial scans, and the imaging time is 107 ms. 31
3.16 Three-dimensional imaging results for the macular hole patient. A: Fundus projection, B: horizontal scanning image, C: virtual vertical scanning image, and D: virtual *en-face* slice are shown. In the *en-face* slice (D), honeycomb pattern of cysts is appeared (white arrows). 32

4.1 The diagram of the bulk motion artifact elimination algorithm. $\phi_i(z), \phi_i'(z)$: phases of i-th axial scan before elimination and after elimination, respectively, $\Delta\phi_i(z)$: phase differences, $\Delta\phi_i^{bulk}$: the phase difference corresponding to the phase shift from 0-th axial scan due to the bulk motion of the sample. PW: phase wrapping process. . . . 35
4.2 Comparison of histograms with different number of histogram bins. N: number of histogram bins, M: the number of histograms used in the averaging process. The histogram bin width of each histogram is determined by (a) the phase noise and (b), (c) the Freedman & Diaconis rule. (c) is the averaged shifted histogram using eight histograms. (d) is a conventional histogram with a histogram bin width equivalent to that of the histogram in (c). 37
4.3 Comparison of the blood flow images after bulk motion elimination using different histogram bin width determination methods. Phase-noise-based method (A) and the Freedman & Diaconis rule (B), (C) are used to determine the histogram bin width. An averaged shifted histogram is used for (C). The white and yellow arrows indicate the bulk motion artifacts due to the estimation error. The images consist of 1024 axial scans and cover 1.5 mm in the transversal direction. The black and white colors denote Doppler shifts of -5.6 and +5.6 kHz, respectively. 38
4.4 Three-dimensional optical coherence angiography of the macular region. The fundus projection image of the 3D OCT volume set (A) and the sequence of the OCT images (B) are shown. The segmented anterior (red) and posterior (blue) boundaries of the tissue and the high reflectivity layer (green) are indicated in the OCT images (B). The volume rendering images (E) and (F) are produced from stacks of bi-directional flow images (C) and the power of Doppler shift images (D). The composite volume rendering image (G) is a combination of the retinal part of (E) (encoded in cyan) and the choroidal part of (F) (encoded in yellow). The image size is 5 mm × 5 mm, corresponding to 1024 × 138 axial scans. Multimedia files are available on http://www.opticsexpress.org/abstract.cfm?id=97672 41

4.5 Three-dimensional optical coherence angiography of the ONH. (A): volume rendering image of the bi-directional flow volume set (upper left), (B): volume rendering image of the power of Doppler shift volume set, (C): the composite volume rendering image of the retinal part of (A) (cyan) and the choroidal part of (B) (yellow). The image size is 5 mm × 5 mm, corresponding to 1024 × 138 axial scans. Multimedia files are available on http://www.opticsexpress.org/abstract.cfm?id=97672 42
4.6 Optical coherence angiography of the macula lutea of the human eye. Each image is produced by the integration of (A) the entire depth, (C) tissue region, (D) retinal part, and (E) choroidal part of the power of Doppler shift images. (F) is a combination of (D) and (E). In the cross-sectional flow image (B), each integration range is indicated. 44
4.7 Optical coherence angiography of the ONH of the human eye. Each image is produced by the integration of (A) the entire depth, (C) tissue region, (D) retinal part, and (E) choroidal part of the power of Doppler shift images. And (F) is a combination of (D) and (E). In the cross-sectional flow image (B), each integration range is indicated. 45
4.8 Comparison of the angiographies of the macula lutea. From the left-hand side, the images of the fundus photography (A), FA (B), and ICGA (C) are shown. Two-dimensional OCA image (D) is cropped to compare it with to the other angiographies (E). The retinal vessels and some choroidal vessels appear in (D), which is in agreement with FA (B) and ICGA (C). The size of the image (E) is 5 mm × 3.6 mm (horizontal × vertical). 46
4.9 Comparison of the angiographies of the ONH. From the left-hand side, the images of the fundus photography (A), FA (B), and ICGA (C) are shown. Two-dimensional OCA image (D) is cropped to compare it with the other angiographies (E). The retinal vessels and some choroidal vessels appear in (D), which is in agreement with FA (B) and ICGA (C). The size of the image (E) is 5 mm × 3.6 mm (horizontal × vertical). 47
4.10 Composite image with shadowgram and flow projection image. As compared to the power of Doppler shift projection of the retinal part (A), the shadowgram (B) exhibits a fine retinal vasculature. The composite colored angiograms (C), (D) are obtained from the power of Doppler shift projection of the choroidal part (Fig. 4.6 (C)) and (A) or (B), respectively. 49

Acronym

OCT Optical coherence tomography

TD-OCT Time-domain optical coherence tomography

SD-OCT Spectral-domain optical coherence tomography

OCA Optical coherence angiography

FWHM Full width at half maximum

BS Beam splitter

SLD Superluminescent diode

CCD Charge-coupled device

ONH Optic nerve head

RNFL Retinal nerve fiber layer

GCL Ganglion cell layer

IPL inner plexiform layer

INL inner nuclear layer

OPL outer plexiform layer

ONL outer nuclear layer

ELM External limiting membrane

IS/OS inner/outer segments junction

RPE retinal pigment epithelium

CC choriocapillaris

UHR-SD-OCT Ultrahigh-resolution spectral-domain optical coherence tomography

Chapter 1

Introduction

1.1 Overview

Medical imaging has had a sigificant impact on medical diagnosis. It assists medical doctors in diagnosing diseases and abnormalities and in checking treatments. The rise of modern medical imaging can be attributed to the development of key technologies.

In the past decade, technological advances in the fields of fiber optics, light sources, optical detectors, and so on, have resulted in the development of a new biomedical imaging modality called optical coherence tomography (OCT) [1]. OCT has a high spatial resolution and can be used for non-invasive imaging the cross-section of biological tissues in the range of several millimeters. The applications of OCT extend to several clinical and biological fields, e.g., ophthalmology [2], dermatology [3], gastroenterology [4], cardiology [5], dentistry [6], and neurology [7]. The rapid advancement of OCT technology has led to thedevelopment of ultrahigh-resolution imaging [8] and high-speed real-time imaging [9]. Furthermore, functional imaging has been developed for investigating polarization properties [10; 11] and blood flow [12; 13; 14; 15] and as a means of spectroscopic imaging [16; 17; 18].

During OCT development another modality called spectral-domain OCT (SD-OCT) was introduced [19], which could overcome the limitations of conventional OCTs; further, it proved its ability to perform *in vivo* imaging [20]. The advantage of SD-OCT over conventional time-domain OCT (TD-OCT) with regard to sensitivity has been suggested [21; 22; 23] and proved experimentally [24]. This crucial advantage allows high-speed imaging with a high signal-to-noise ratio, which can be realized by using modern high-speed CCD cameras [24; 25].

1.2 Spectral-domain optical coherence tomography

In SD-OCT systems, backscattered low-coherence light is mixed with a reference beam by an interferometer then, each spectral component is separated by a grating-

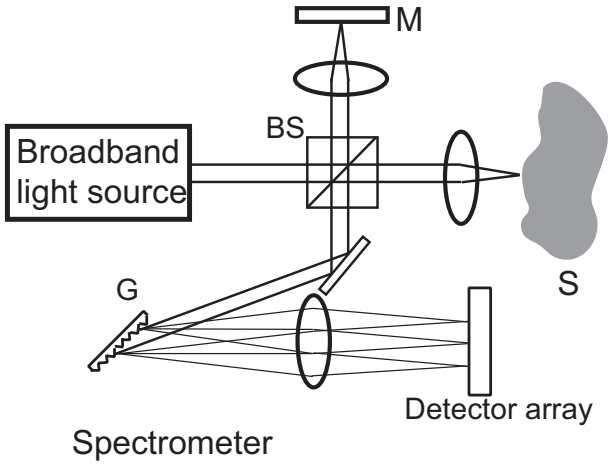

Figure 1.1: Schematic diagram of SD-OCT

based spectrometer and detected using a linear detector array. The detected signal is expressed as

$$I(k) = S(k)|\sqrt{R_r}r_r + \sqrt{R_s}\int a_s(z)e^{-ikz}dz|^2, \tag{1.1}$$

where $I(k)$ denotes the detected spectrum; $S(k)$, the power spectrum of light source; r_r, the amplitude reflectivity of the reference arm; and $a_s(z)$, the axial profile of the amplitude backscattering coefficient of the sample. R_r and R_s denote the total power splitting ratios of the reference beam and the sample beam from the light source to the detection arm. The phase term e^{-ikz} denotes the phase-offset due to the optical path length difference between the reference beam and the backscattered beam. In order to reconstruct the axial profile $a_s(z)$, the spectrum is inverse Fourier transformed so that it can be described by the expression

$$\begin{aligned}\mathscr{F}_k^{-1}[I(k)](z) = P_0V(z/c) \otimes \Big[&R_r|r_r|^2\delta(z) + R_sAC_z(a_s(z)) \\ &+\sqrt{R_rR_s}r_r^*a_s(z) + \sqrt{R_rR_s}r_ra_s^*(-z)\Big],\end{aligned} \tag{1.2}$$

where $V(z)$ is the temporal coherence function of the light source ($V \ni [0,1]$), $\mathscr{F}_z[](k)$ is the Fourier transform from z-space to k-space, and $AC_z()$ is the auto-correlation function along the z-direction. The first two terms are the autocorrelations of the reference beam and backscattered beam, respectively.

The third term shows the sample structure, and the fourth term is the reversed signal of the third term at $z = 0$. When the image crosses over the zero delay, $z = 0$, the auto-correlation terms and the reversed image overlap. The offset of the path length difference is constantly added in the interferometer to separate the real image from the coherent ghost images so that the half of the axial range is occupied.

1.2.1 Resolutions

OCT is a depth-resolved imaging technique that utilizes a low-coherence light source to enable the extraction of backscattered light from certain depths in biological tissues. SD-OCT works on the same concept, and the definitions and limitations of the spatial resolutions of SD-OCT and TD-OCT are the same.

OCT (also SD-OCT) is usually implemented using a fiber-optic interferometer. Therefore, the confocal effect is caused by an optical fiber. The combination of high conforcality and coherence gating allows high selectivity of backscattered light around the focusing point [26]. The axial resolution is determined by coherence length of the broadband light source. If the light source spectrum has a Gaussian shape, the axial resolution is given by [27],

$$\delta z = \frac{2\ln 2}{n\pi}\frac{\lambda_0^2}{\Delta\lambda_{FWHM}}, \tag{1.3}$$

where λ_0 is the central wavelength; $\Delta\lambda_{FWHM}$, the full width at half maximum (FWHM) of the light source spectrum; and n, the refractive index of tissue.

On the other hand, the lateral resolution depends on the beam spot size on the samples in an identical manner to the dependence observed in laser imaging techniques. If the beam shape is assumed to be Gaussian profile, the beam diameter on the focusing plane, Δx, is expressed as [27]

$$\Delta x = \frac{4\lambda_0}{n\pi}\frac{f}{d}, \tag{1.4}$$

where f denotes the focal length of the objective lens and d denotes the beam diameter on the lens. This is the lateral resolution only for the in-focus case. Defocusing causes a large beam diameter. The depth-of-focus is defined to be twice the $Rayleigh - range$, and it can be expressed as,

$$2z_R = \frac{\pi\Delta x^2}{2\lambda_0}. \tag{1.5}$$

1.2.2 Sensitivity advantage

The main advantage of SD-OCT over the conventional TD-OCT is higher sensitivity. Several studies have reported this sensitivity advantage [21; 28; 22; 23; 29]. This advantage is briefly described as follows.

TD-OCT extracts the backscattered light only from within the coherence gate, while backscattered light also exists outside the gate. Thus, this light does not contribute toward the signal. In contrast, SD-OCT detects the backscattered light from the entire depth range parallely (not directly, but with frequency-domain detection); consequently, SD-OCT exhibits high sensitivity superior to that of TD-OCT.

The comparison between the sensitivities of both systems is described as follows.

Sensitivity of SD-OCT

From the signal-to-noise ratio of SD-OCT, (Appendix A), the sensitivity of SD-OCT can be expressed as,

$$\mathscr{S}_{SD} = \frac{SNR_{SD,max}}{SNR_{SD,min}} \tag{1.6}$$

Since SD-OCT is characterized by parallel detection in the frequency-domain, the integration time is relatively long; thus, shot noise dominates the intensity noise [30]. The sensitivity approaches the photon shot noise limit even with high-speed imaging and without balanced detection [24]. The shot-noise-limited sensitivity of SD-OCT is givien by

$$\mathscr{S}_{SD}^{shot} = \frac{\eta\tau}{h\nu_0}\epsilon P_s, \tag{1.7}$$

where $\epsilon P_s = R_s P_0$, P_s is the power of light illuminating the sample and ϵ is the parameter of the interferometer and is defined as the efficiency of light transmitted from the probing arm to the detection arm.

Sensitivity of TD-OCT

In TD-OCT, the excess photon noise will dominates photon shot noise for the conditions of high-speed detection [31]. Thus, balanced detection is required for shot-noise-limited detection. The shot-noise-limited sensitivity of TD-OCT is defined as [32]

$$\mathscr{S}_{TD}^{shot} = \frac{\eta\epsilon P_s}{h\nu_0 BW}, \tag{1.8}$$

where BW denotes the detection bandwidth.

For comparison, we assume that the same light source and configuration of the interferometers are used and that the quantum efficiencies of the detectors are the same i.e. P_0, ν_0, ϵ, and η are the same. If the spectrum of the light source has a Gaussian shape, the optimal BW can be expressed as[9]

$$BW = 2\frac{\Delta\lambda_{FWHM} V_g}{\lambda_0^2}, \tag{1.9}$$

where V_g denotes the group velocity induced by an optical delay-line. When the depth is scanned with a constant V_g by TD-OCT; and the observation time of one axial scan and the ranging depth are the same, the relationship between the detection bandwidth BW and the integration time τ is givien by

$$BW = 2\frac{\Delta\lambda_{FWHM}}{\lambda_0^2}\frac{nZ_{RD}}{\tau}, \tag{1.10}$$

where Z_{RD} is the ranging depth and n is the refractive index of tissues. By using the ranging depth of SD-OCT [eq. (1.12)], the relationship between the shot-noise-limited sensitivities of SD-OCT and TD-OCT is expressed as

$$\mathscr{S}_{SD}^{shot} = \frac{1}{2}\frac{\Delta\lambda_{FWHM}}{\Delta\lambda}\mathscr{S}_{TD}^{shot}. \tag{1.11}$$

In eq. (1.11), the factor is proportional to the ratio of the ranging depth to the axial resolution $\Delta\lambda_{FWHM}/\Delta\lambda \sim Z_{RD}/\delta z$. Thus, the sensitivity gain of SD-OCT over TD-OCT become larger with the condition of the deep ranging depth and the high axial resolution.

1.2.3 Axial range limitations

The measurable axial range of SD-OCT is limited by the sampling interval of wavelength. In contrast, in TD-OCT, it is defined by the scanning range of the optical delay-line. The ranging depth is defined as [19]

$$Z_{RD} = \frac{\lambda_0^2}{4n\Delta\lambda}, \tag{1.12}$$

where $\Delta\lambda$ denotes the sampling interval of wavelength defined by the detector separation of a linear detector array.

One of drawbacks of frequency-domain detection is the signal decay, which is dominated by spectrometer resolution. The point spread function in the frequency domain corresponds to the window function in the time domain so that the signal intensity depends on the depth, although the reflectivity is the same. The formula of the reduction is provided by Yun et al. [33] as

$$R(z) = \left(\frac{sin\zeta}{\zeta}\right)^2 \exp\left[-\frac{w^2}{2\ln 2}\zeta^2\right], \tag{1.13}$$

where $\zeta = (\pi/2)(z/Z_{RD})$ is the normalized depth and $w = \delta\lambda/\Delta\lambda$, where $\delta\lambda$ is the resolution of the spectrometer.

1.3 Aim of thesis

In this dissertation, the fundamental limitation of SD-OCT and one of its solutions are discussed in Chapter 2, and the applications of SD-OCT are described in Chapters 3 and 4. In Chapter 3, a high-speed ophthalmic SD-OCT system used for *in vivo* human eye imaging is demonstrated. Further, the 3D vasculature imaging of the human eye is explained in Chapter 4.

Chapter 2

High-speed complex spectral-domain optical coherence tomography*

Although SD-OCT is a promising imaging modality, it is problematic in terms of coherent ghost images. An SD-OCT image is computed from a measured spectral interferogram, namely, the joint "power" spectrum of a probe beam and a reference beam by digital Fourier transform. Hence, the resulting SD-OCT image consists of not only a primary OCT image but also the conjugate of the OCT image and two auto-correlation of the probe beam and the reference beam. These auto-correlations and the conjugate image, referred to as coherent ghost images. The offset of path length difference is constantly added in an interferometer to separate the real image and the conjugate image so that the half of the axial range is occupied. Furthermore, the region around zero path length difference is discarded to reject auto-correlation terms. This region is the most sensitive region since the signal-to-noise ratio is decreased as path length difference is increased (Sec. 1.2.3). This problem will be more serious with ultra-broadband light source since to maintain the spectrometer's resolution demands the large number of elements in a linear detector array.

A complex SD-OCT using a phase-shifting method (phase-shifting SD-OCT) has been reported to eliminate coherent ghost images[34]. In this complex SD-OCT, a complex spectrum is calculated from several, typically five, spectral interferograms, which are obtained with different phase offsets of the reference beam using a phase shifting algorithm[35; 36]. Although this complex SD-OCT completely eliminates the coherent ghost images, it requires several measurements for an OCT image and sacrifices the short measurement time. Although an im-

*The portions of this chapter have been published in the following article:
Y. Yasuno, S. Makita, T. Endo, G. Aoki, M. Itoh and T. Yatagai, "Simultaneous B-M-mode scanning method for real-time full-range Fourier domain optical coherence tomography," Applied Optics **45**, 1861-1865, (2006). http://ao.osa.org/abstract.cfm?id=88199

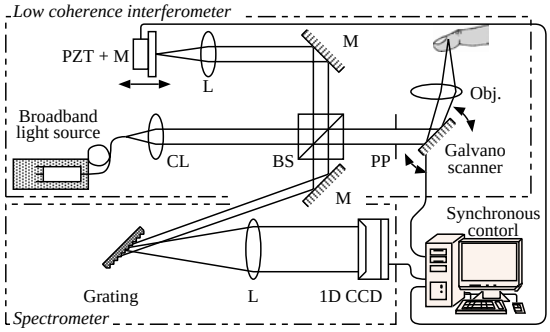

Figure 2.1: Optical scheme of a complex SD-OCT. CL: collimator lens, Ls: lenses, Obj.: objective lens, BS: beam splitter, PS: pupil stop, and PZT: piezoelectric transducer. The broadband light source is an SLD with a 828 nm central wavelength and a 40 nm band width. The CCD camera is a line-scan CCD camera with 2048 pixels.

proved version of the phase-shifting algorithm for a high-speed SD-OCT has also been proposed, it still requires two measurements for a single full-range SD-OCT image[37; 38].

In this chapter, we present a method for a complex SD-OCT to eliminate the coherent ghost images without sacrificing the short measurement time. Our SD-OCT modulates the phase offset of the reference beam (M-scan) and laterally scans the probing beam (B-scan) simultaneously to obtain a two-dimensional (2D) spectral interferogram; here, the two dimensions are that of the lateral position and optical frequency. Each lateral 1D component of this 2D spectral interferogram is processed by the Fourier transform method (FTM)[39]. This operation results in a 2D complex spectrum, and this complex spectrum leads to a full-range SD-OCT image which is free from coherent ghost images. This SD-OCT determines a full-range SD-OCT image without any additional acquisition time for M-scan, thus taking only an identical measurement to that of non-complex SD-OCT.

2.1 Overview of complex SD-OCT

Our simultaneous B-M-mode scan complex SD-OCT (BM-scan SD-OCT) is highly similar to the phase-shifting SD-OCT in terms of their basic concepts. Both use a complex spectrum to eliminate the ghost images, the difference being in the manner in which they obtain the phase information of the complex spectrum. Furthermore, the two above-mentioned complex SD-OCTs have rather similar optical setups; hence, it is convenient to first review the principle of phase-shifting SD-OCT to understand the BM-scan SD-OCT.

The optical scheme of phase-shifting SD-OCT is shown in Fig. 2.1. The light source is a broadband light source, e.g., a super luminescent diode (SLD) or a femtosecond pulse laser. In our SD-OCT, we used an SLD with a central wavelength of

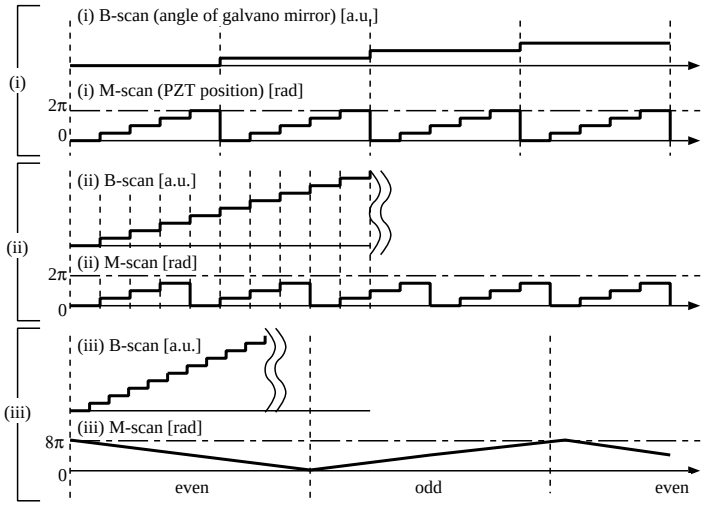

Figure 2.2: Time charts of B-scans and M-scans for (i) a conventional phase-shifting SD-OCT, (ii) a BM-scan SD-OCT and, (iii) the modified BM-scan SD-OCT.

828 nm and 44.7 nm band width. The incident light is split into a reference beam and a probe beam by a beam splitter (BS). The reference beam is reflected back by a reference mirror, and the probing beam is reflected and scattered back by the sample being measured. These two beams interfere with each other in the spectral domain, and form a spectral interferogram on the CCD of

$$\tilde{I}(\omega) = |\tilde{p}(\omega)|^2 + |\tilde{r}(\omega)|^2 + 2\,|\tilde{p}(\omega)|\,|\tilde{r}(\omega)|\cos\left(\angle\tilde{p}(\omega) + \varphi\right), \qquad (2.1)$$

where $\tilde{r}(\omega)$ and $\tilde{p}(\omega)$ are the temporal Fourier transforms of $r(t)$ and $p(t)$, respectively temporal complex profiles of the reference and the probing beams. $\angle\tilde{p}(\omega)$ is the relative phase-angle of $\tilde{p}(\omega)$ to the phase-angle of $\tilde{r}(\omega)$, and φ is the phase offset employed for the phase-shifting method described below. Here, $p(t)$ has the depth-structure information of the sample such that $t = 2z/v$ (v is the speed of light in the sample, and z is the axial position).

The phase offset φ in eq. (2.1) is modulated by a piezoelectric transducer (PZT), in a manner illustrated in Fig. 2.2-(i) (M-scan). This figure shows that φ changes to several (typically 5) phase values for a single A-scan. A phase-shifting algorithm retrieves the phase distribution of the spectrum from these spectra with different phase offsets[35; 36]. The above-mentioned derived complex spectrum is then digitally 1D Fourier transformed along the ω-axis, and this procedure finally results in a full-range SD-OCT image.

We reiterate that this phase-shifting method requires several interferograms (several M-scans) for each single A-scan. It is clear that the phase-shifting SD-OCT results in a longer measurement time than that of a non-complex SD-OCT.

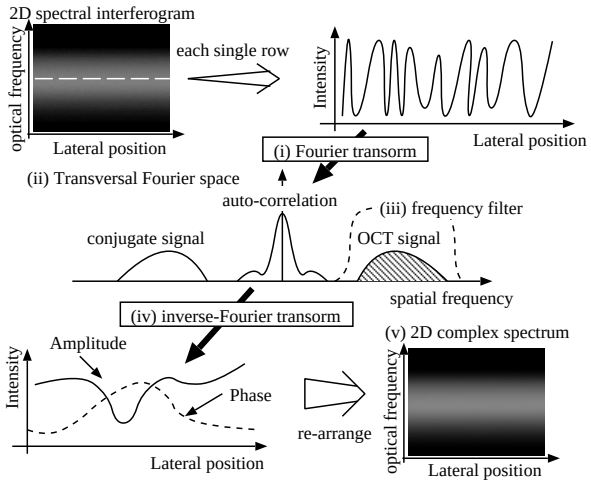

Figure 2.3: A flow diagram of the phase reconstruction procedure of a BM-scan SD-OCT.

2.2 Simultaneous BM-mode scanning

In contrast with the phase-shifting SD-OCT, the phase modulation of the BM-scan SD-OCT is performed in the manner illustrated in Fig. 2.2-(ii). Here, the phase step between two M-scans is $\pi/2$ rad, and the B-scan and M-scan are performed simultaneously; hence, the measurement time required to obtain a 2D spectral interferogram is identical to the measurement time of a non-complex SD-OCT. A full-range SD-OCT image is calculated from this single 2D spectral interferogram in the following manner.

The 2D spectral interferogram is expressed as

$$\tilde{I}(x,\omega) = |\tilde{p}(x,\omega)|^2 + |\tilde{r}(\omega)|^2 + \tilde{p}(x,\omega)\tilde{r}^*(\omega)\exp\{i\varphi(x)\} + c.c. \tag{2.2}$$

where $c.c.$ is the complex conjugate of the 3rd term on the right-hand side of this equation, x corresponds to the transversal position of the B-scan, and * denotes the complex conjugate of the concerned term. The modulation of $\varphi(x)$ is now a function of x because of the simultaneous BM-scan, and $\varphi(x) = \beta x$ according to the modulation of the PZT shown in Fig. 2.2-(ii). Here, β is the gradient of the phase modulation defined in order to achieve modulation step of $\pi/2$ rad.

In the first step, the 2D spectral interferogram is digitally 1D-Fourier transformed along x, as shown in Fig. 2.3-(i), as

$$\begin{aligned}\mathcal{F}_x\left[\tilde{I}(x,\omega)\right] = \Gamma_u\left[\mathcal{F}_x\left[\tilde{p}(x,\omega)\right]\right] + |\tilde{r}(\omega)|^2\,\delta(u) \\ + \mathcal{F}_x\left[\tilde{p}(x,\omega)\tilde{r}^*(\omega)\right] * \delta(u-\beta) \\ + \mathcal{F}_x\left[\tilde{p}^*(x,\omega)\tilde{r}(\omega)\right] * \delta(u+\beta)\end{aligned} \tag{2.3}$$

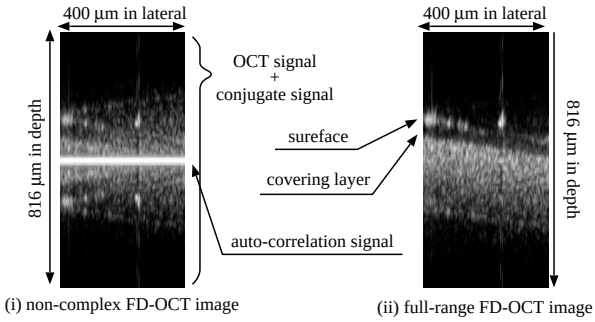

Figure 2.4: (i) Non-complex SD-OCT image, and (ii) the complex BM-scan SD-OCT image of a plastic plate with a covering layer.

where u is the Fourier conjugate of x, $\Gamma_u[\cdot]$ and $*$ are a correlation operator and a convolution operator along u, respectively, and $\mathcal{F}_x[\cdot]$ denotes the Fourier transform operator along x. We used an autocorrelation theorem of Fourier transform[40] for the first term of the right-hand-side of this equation.

The third term on the right-hand side of eq. (2.3) contains information regarding the OCT image, the fourth term on the right-hand side of eq. (2.3) is the conjugate of the third term, and the first and second terms on the right-hand side of eq. (2.3) correspond to the auto-correlation signals. Here, the above-mentioned terms are distinct from each other in the u-domain, because of the carrier frequency originating in the M-scan, as shown in Fig. 2.3-(ii).

We clip out only the third term, namely, the information regarding the OCT signal, by a window function (Fig. 2.3-(iii)) and subsequently inverse Fourier transform it to the original domain (Fig. 2.3-(iv)).

After this procedure, we obtain a complex 2D spectrum as

$$\tilde{I}(x,\omega) = \tilde{p}(x,\omega)\tilde{r}^*(\omega)\exp(i\beta x) \tag{2.4}$$

as shown in Fig. 2.3-(v), that is, identical to the complex spectra obtained from the phase-shifting SD-OCT but extracted from only one 2D spectral interferogram. This phase-retrieval procedure is referred to as the Fourier transform method (FTM)[39] and has been widely employed in monochromatic interferometers and fringe projection profilometers.

Figure 2.4 shows a full-range BM-scan SD-OCT image of a static sample; a plastic plate with a covering layer. Figure 2.4-(i) shows the SD-OCT image without the phase retrieval procedure and Fig. 2.4-(ii) shows the image with this phase retrieval procedure. The coherent ghost images have been clearly eliminated and the covering layer is visualized.

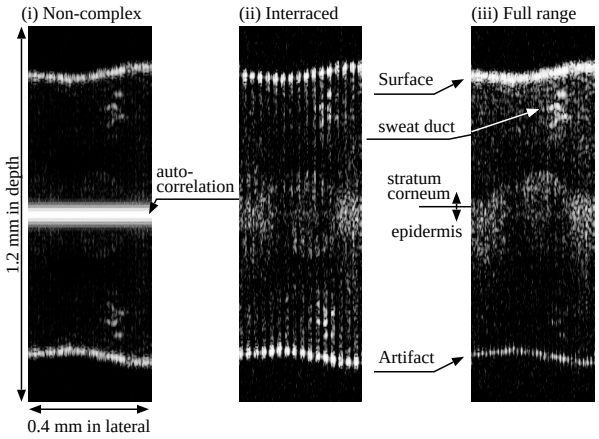

Figure 2.5: (i) Conventional non-complex, (ii) interlaced full-range, and (iii) full-range SD-OCT images of an *in vivo* sweat duct in a human finger pad taken with an acquisition time of 27 ms.

2.3 High-speed BM-mode scanning

In principle, this BM-scan method is applicable for a high-speed complex SD-OCT, however, in practice, the M-mode scanning by a PZT restricts measurement speed. Since a PZT is a relatively slow device in comparison to a CCD camera for A-scans, the frequency of the saw-tooth modulation of the PZT shown in Fig. 2.2-(ii) is not sufficiently high in order to match the maximum A-scan speed, which is determined by the speed of the CCD camera. For example, the SD-OCT took a few minutes to obtain the image of Fig. 2.4, which is clearly unsuitable for *in vivo* measurements.

In order to achieve a high-speed complex SD-OCT, we introduce modified M-mode scanning. The time-chart of this method is shown in Fig. 2.2-(iii). Here, the M-scan is performed using a triangular wave. The repetition frequency, which is restricted for mechanical reasons, is significantly larger than the case wherein saw-tooth modulation is employed. Hence it has become possible to achieve complex SD-OCT measurements with the maximum speed of the CCD camera, 18.7 k A-scans/sec in our prototype.

We measured a 2D spectral interferogram of an *in vivo* human finger pad with the modified triangular M-scan. If we did not apply any phase-retrieval algorithm to the 2D interferogram, we could obtain an OCT image with coherent ghosts, as shown in Fig. 2.5-(i).

To obtain a full-range SD-OCT image, the acquired 2D spectral interferogram is signal-processed in a manner identical to the normal BM-scan SD-OCT described in the former section. Here, we recall that we are using a triangular M-mode modulation. To understand the effect of this M-mode modulation, it is convenient to categorize each area of this modulation function as shown in Fig.

2.2-(iii); namely, the even and odd fields. In the even field, the derivative of the M-mode modulation is negative; hence the complex conjugate of the OCT signal shifts into the positive frequency area after the first 1D Fourier transform, and this conjugate signal is selected by the frequency filter. Similarly, in the odd field, the primary OCT signal shifts into the positive frequency area and is selected. This procedure provides an interlaced full-range OCT image as shown in Fig. 2.5-(ii).

This interlaced OCT image is divided into even and odd fields. Subsequently, the even field is flipped over, and finally we obtain a full-range SD-OCT image on recombining the two fields as shown in Fig. 2.5-(iii). Here, we observe the border of the stratum corneum and epidermis, along with a sweat duct in the finger pad. There are artifacts of the surface reflection at the turning points of the M-mode modulation since at these points, the phase modulation amplitude approaching to zero.

Here, the acquisition time of this OCT image is identical to a conventional non-complex SD-OCT, in which the acquisition time is restricted by the acquisition time of a CCD camera. Our prototype system is capable of taking 18 frames/sec full-range SD-OCT movie with an acquisition time of 27 ms for a single frame, and each frame consists of 2048 pixels in depth and 512 A-scans. The disagreement of the frame-rate and acquisition time is due to time-loss for data transmission and data storage.

2.4 Discussion

This BM-scan SD-OCT requires a fine transversal sampling period. Signal broadening occurred after the first 1D discrete Fourier transform is clearly observed since the lateral beam scanning causes signal fluctuation. The phase modulation performed has a gradient of $\pi/2$ rad/A-scan. This gradient sets the centers of the OCT signal and the conjugate signal to $\frac{1}{4}N$ and $\frac{3}{4}N$, respectively, in the numerical transversal Fourier domain. Here, N is the number of axial scans in a single cross-sectional image, i.e., it is the number of sampling points in the numerical transverse Fourier domain. Thus, the widths of the OCT signal and the conjugate signal must be narrower than $\frac{1}{2}N$, which corresponds to the separation of the two signals. Otherwise, the above mentioned two signals overlap, and it is not possible to split them in the transverse Fourier domain.

The high-speed complex SD-OCT system is achieved by using the triangular phase modulation waveform. However, the conjugate ambiguities cannot be resolved at the turning points of the modulation curve, as shown in Fig. 2.5-(iii), due to a low phase modulation amplitude at these points. This problem can be resolved by processing the complex SD-OCT algorithm for each modulation field or by modifying the beam scanning protocol.

2.5 Summary

We developed a high-speed full-range SD-OCT system. This OCT uses the Fourier transform method to retrieve the phase information of a 2D spectral interferogram, and provides a full-range SD-OCT image with an acquisition time similar to that of a non-complex SD-OCT. This BM-scan SD-OCT has been applied to *in vivo* measurements and it provided a full-field SD-OCT image with an acquisition time of 27 ms.

Chapter 3

Retinal imaging by spectral-domain optical coherence tomography*

The eye is a part of the vision system, which forms and detects an outside of image. The light sensor of the eye is the retina. It has a multilayered structure which is consisting of several types of neurons. Each layer has a thickness of several hundred microns. They convert light energy to electric energy, process, and transfer electric impulses to the brain. Abnormalities in the retina cause visual damage. The worst case of an eye disease is vision loss. Retinal diagnosis techniques are one of the main parts of the clinical ophthalmology.

OCT is a powerful diagnostic tool for ophthalmology because its high axial resolution resolves the layered retinal structure [2]. By using SD-OCT, high-speed retinal cross-sectional imaging is achieved [24]. Subsequently, high-quality imaging of the retinal cross-section and 3D retinal imaging become possible and can be used to develop the retinal disease diagnosis at a high definition.

3.1 Ophthalmic high-speed SD-OCT

For retinal imaging, we constructed a high-speed SD-OCT system with an 840-nm band light source. The schematic of the developed system is shown in Fig. 3.1. A superluminescent diode (Superlum, Russia, SLD-37) is used as the light source; this SLD has a center wavelength of 840 nm and FWHM spectral bandwidth of 50 nm. A free-space optical isolator is placed immediately after the light source. The beam is split by a 20/80 fiber coupler, and 20% of the beam is guided to the sample arm. A 78D lens is used to deliver the beam to the posterior part of the human eye.

*The portions of this chapter have been published in the following article:
S. Makita, Y. Hong, M. Yamanari, T. Yatagai and Y. Yasuno, "Optical coherence angiography," Optics Express **14**, 7821-7840, (2006). http://www.opticsexpress.org/abstract.cfm?id=97672

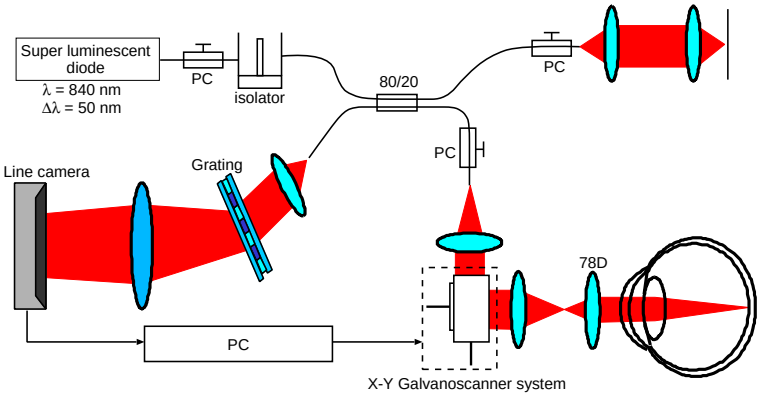

Figure 3.1: Schematic of a high-speed spectral-domain OCT system

The head of the volunteer is fixed on a handmade stage. There is a fixation target to stabilize the other eye that is not imaged by OCT. The optical power of the beam on the cornea is 700 μW, which is lower than the ANSI exposure limit[41]. The beam diameter on the cornea is set to $\sim$ 0.6 mm in FWHM in order to suppress the effect of eye aberrations and obtain a large confocal parameter. The spot size on the retina is calculated to be $\sim$ 30 μm, and the confocal parameter in the tissue is 2 mm (n = 1.38). In the detection arm, the backscattered signal light and reference light are combined and guided to the spectrometer that consists of a transmission grating (Wasatch Photonics, 1200 lp/mm), achromatic lens (f = 200 mm), and high-speed line-scan CCD camera (Basler, L103k-2k). The CCD camera detects the spectral interference signals.

First, the detected spectrum is processed to eliminate the periodic electronic noise with a period of 4 pixels. This noise appears in OCT images as a fixed-pattern noise. Since this noise is unstable in phase, it cannot be eliminated with fixed-pattern noise rejection by using an averaged spectrum, which is mentioned later. Alternatively, a Fourier harmonic of the spectrum at a frequency of 1/4 pixel^{-1} (period of 4 pixels) is obtained and subtracted from the spectrum. Other optical fixed-pattern noises are eliminated by using the averaged spectrum of all the spectra in one image [25]. The nonlinearity of the spectrometer is obtained by analyzing the spectral phase of the OCT signal from a single reflection plane. Then, the spectrum is linearly resampled in k-space (Appendix B). Digital inverse Fourier transform of this spectrum yield a complex signal of an axial profile. To compensate the dispersion mismatch between the two interferometer arms, a numerical automatic algorithm is applied that described in Sec. 3.2.1.

This system performs OCT imaging with an axial scan rate of 18.7 kHz. The exposure time of one axial scan is 53.1 μs. Two-dimensional tomographic imaging with 1024 axial scans is achieved at a frame rate of 18 fps, and a 3D volume comprising 1024 $\times$ 140 axial scans is obtained within 7.7 s. The axial resolution is estimated to be 6.2 μm in air, whereas the measured axial resolution is 8.8 μm

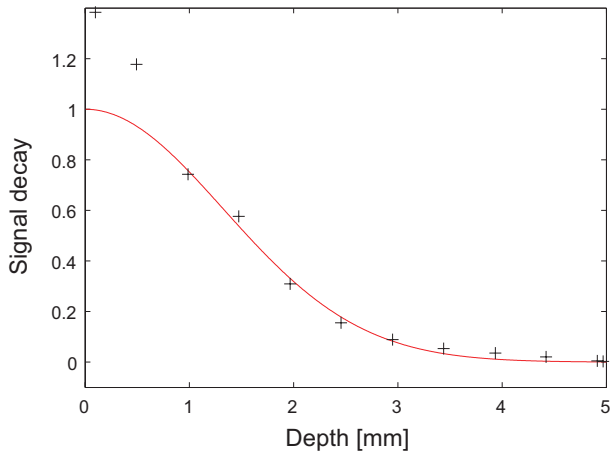

Figure 3.2: Depth-dependent signal-to-noise ratio decay of the ophthalmic SD-OCT system.

in air. This correspond to 6.4 μm in tissues, where the refractive index is assumed to be 1.38. This discrepancy from the theoretical value may be due to the non-Gaussian shape of the source spectrum. The sensitivity of this system is measured to be 99.3 dB at a depth of 100 μm; this value reduces to 92.9 dB at a depth of 2 mm. According to eq. (1.11), the SNR gain compared to TD-OCT is 28.5 dB by using 0.035 nm wavelength separation and 50 nm spectral bandwidth of the light source. This very high gain is achieved by relatively deep ranging depth, i.e. small wavelength separation. Spectrometer's resolution is estimated as 0.066 nm by fitting the curve calculated from eq. (1.13) to measured SNR (Fig. 3.2).

The *in vivo* retinal imaging of the healthy human eye is demonstrated by the developed SD-OCT system. Figure 3.3 shows the 2D SD-OCT image from the optic nerve head (ONH) to the macular region. The image consists of 1000 axial scans, which correspond to an imaging time of 54 ms. For displaying the image, log-compressed OCT intensities are coded on a grayscale colormap (white represents low intensities and black represents high intensities) over a dynamic range of 40 dB, where the minimum value is 5 dB below the noise floor level. Several layers and boundaries appear, such as the retinal nerve fiber layer (RNFL), ganglion cell layer (GCL), inner plexiform layer (IPL), inner nuclear layer (INL), outer plexiform layer (OPL), outer nuclear layer (ONL), external limiting membrane (ELM), inner/outer segments junction (IS/OS), retinal pigment epithelium (RPE), choriocapillaris (CC), and choroid.

3.2 Ultrahigh-resolution SD-OCT

Ultrahigh-resolution ophthalmic OCT can provide high-definition images of retinal diseases [42; 43; 44]. This can be achieved by using an ultra-broadband light

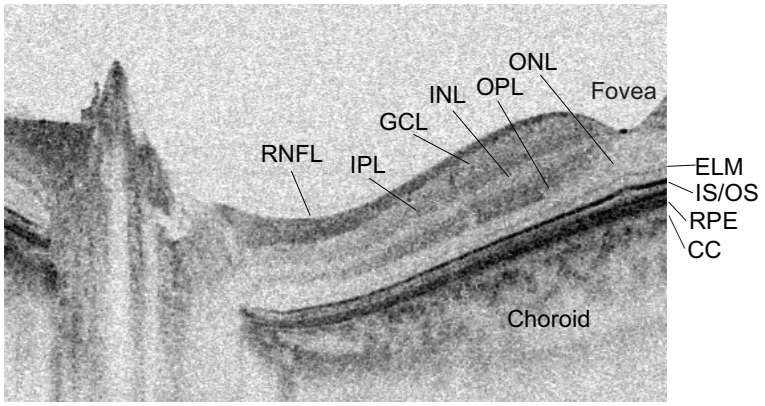

Figure 3.3: SD-OCT image of the human retina *in vivo*. Several retinal structures appear. RNFL: retinal nerve fiber layer, GCL: ganglion cell layer, IPL: inner plexiform layer, INL: inner nuclear layer, OPL: outer plexiform layer, ONL: outer nuclear layer, ELM: external limiting membrane, IS/OS: inner/outer segments junction, RPE: retinal pigment epithelium, CC: choriocapillaris. The image size is 5.6 mm $\times$ 1 mm (lateral $\times$ depth).

source such as a Kerr lens mode-locked (KLM) Ti:Al_2O_3 laser. In SD-OCT, the signal-to-noise ratio is independent of the bandwidth of the light source. Thus, the sensitivity advantage over TD-OCT increases as discussed in sec. 1.2.2 since the signal-to-noise ratio of TD-OCT decreases with an increase in spectral bandwidth. Ultrahigh-resolution SD-OCT (UHR-SD-OCT) has been demonstrated by using a KLM Ti:sapphire laser [45; 30] and a superluminescent diode [46].

A superluminescent-diode-based UHR-SD-OCT system is developed. The superluminescent diode (Superlum, Russia, T870) has a central wavelength and FWHM bandwidth of 870 nm and 170 nm, respectively. It can provide a theoretical axial resolution of $\sim$ 1.4 μm in the tissue. The interferometer configuration is similar to that described in the former section, but the coupling ratio of the fiber-coupler is 10/90. In the spectrometer, a combination lens (f = 110 mm) of two achromatic lenses (f = 200 mm) is used along with a high-speed line CCD camera (Atmel, France, AViiVA M2 CL 2014). The input power to the cornea is 400 μW and the sensitivity is measured as 93 dB at a depth of 80 μm. Spectrometer's resolution is estimated as 0.18 nm by fitting the curve calculated from eq. (1.13) to measured SNR (Fig. 3.4). The actual axial resolution is limited by the wavelength dependency of the fiber coupling ratio, aberrations of the optics in the spectrometer, and low quantum efficiency of the CCD camera for the long-wavelength region; thus, it is $\sim$ 3 μm in the tissues. The axial resolution is almost constant along the depth except near the end of the ranging depth. The depth dependence of axial resolution (in tissue) is shown in Fig. 3.5.

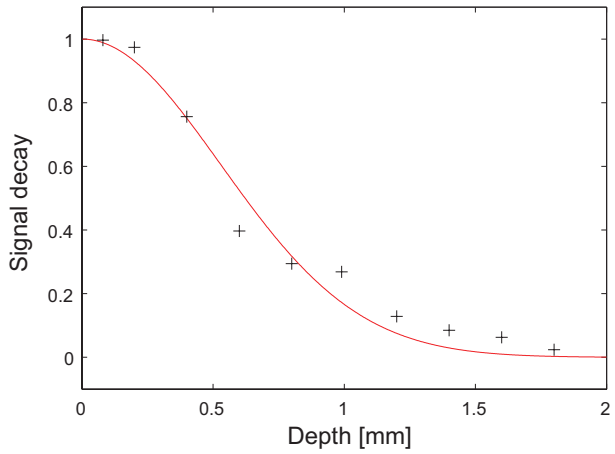

Figure 3.4: Depth-dependent signal-to-noise ratio decay of the UHR-SD-OCT system.

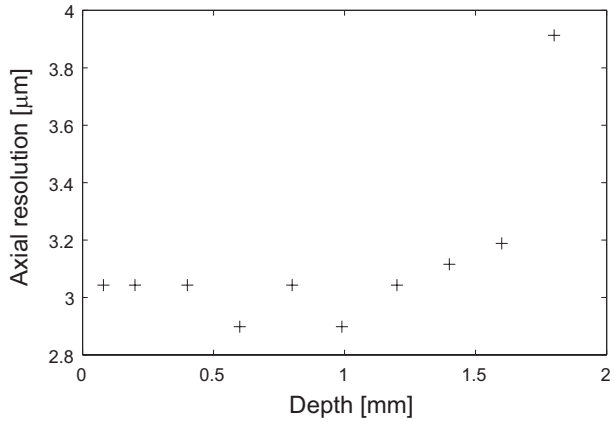

Figure 3.5: Depth dependence of axial resolution in the UHR-SD-OCT system

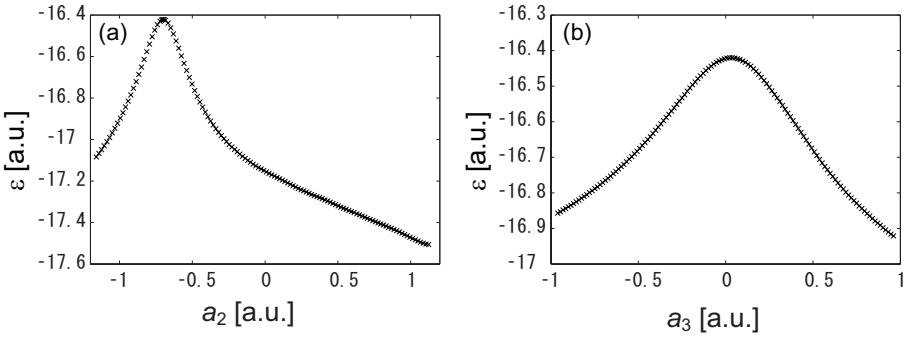

Figure 3.6: Cost function for dispersion compensation. (a) Second-order coefficient, (b) third-order coefficient.

3.2.1 Numerical dispersion compensation

The dispersion mismatch between two interferometer arms causes the broadening of the point spread function of OCT images. Hence, the OCT images will be blurred. This limitation is more serious for UHR-OCT. To balance the chromatic dispersion between the two arms, additional dispersive media such as glasses are introduced [8]. A grating-based rapid optical delay line can also compensate the dispersion [47].

In retinal imaging, there is a thick dispersive medium in the sample arm, namely, the eye. Light traverses a long distance in the anterior eye chamber, lens, and vitreous humor. Thus, a large dispersion mismatch occurs. For bringing about the dispersion compensation of the eye, water with thickness corresponding thickness to the eye length is introduced [48; 30]. However, the extent of eye dispersion depends on the individual due to variable properties of the eye such as the eye length; thus, these hardware-based methods are difficult to adapt to each type of eye.

Numerical dispersion compensation methods that can possibly used to compensate a depth-dependent dispersion are presented [49; 50]. An automatic dispersion compensation based on the numerical method is also demonstrated [51].

Since the numerical methods are suitable for adapting to variable eye lengths, numerical dispersion compensation methods are used for retinal imaging with UHR SD-OCT. Cense et al. obtained dispersion parameters from specular reflection at the fovea [46]. However, this method requires the fovea to be imaged and the specular reflection point to be identified. On the other hand, Wojtkowski et al. proposed automatic dispersion compensation by using iterative optimization [45]. This method assumes that when a dispersion-free condition is achieved, the signal power becomes concentrated and sharpened.

A similar automatic compensation method is used, but with a different cost function.

The dispersion-induced spectral fringes have a frequency-dependent phase,

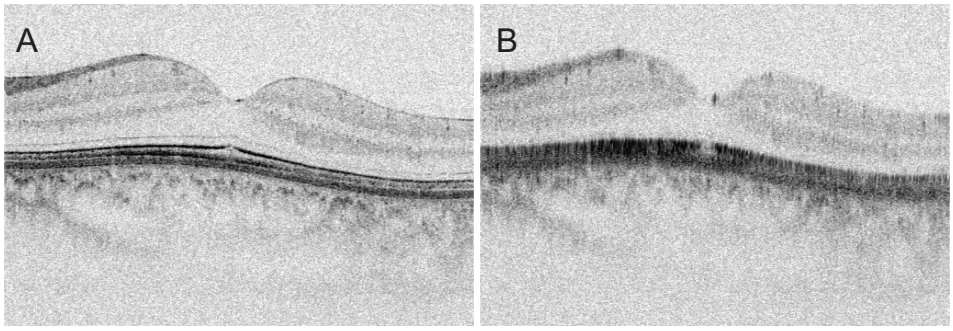

Figure 3.7: Ultrahigh-resolution retinal cross-section (a) with and (b) without dispersion compensation.

which can be expanded by the Taylor series as

$$\phi(k) = \phi(k_0) + \frac{\partial \phi(k)}{\partial k}\Big|_{k_0}(k-k_0) + \frac{\partial^2 \phi(k)}{2\partial k^2}\Big|_{k_0}(k-k_0)^2 + \cdots + \frac{\partial^n \phi(k)}{n!\partial k^n}\Big|_{k_0}(k-k_0)^n. \tag{3.1}$$

The second-order and third-order terms are countered in the spectral fringe in order to suppress the dispersion. For optimization, the sharpness of the image is defined as the negative information entropy of the normalized image intensity, p_{ij},

$$\epsilon = \sum^{i,j} p_{ij} \log p_{ij}. \tag{3.2}$$

The optimum second-order coefficient is estimated by maximizing the cost function using the iterative method; then, the third-order coefficient is optimized. This cost function is very robust since it does not require any parameters and exhibits smooth curves as shown in Fig. 3.6, where coefficients $a_2 = \frac{1}{2}\frac{\partial^2 \phi(k)}{\partial k^2}\Big|_{k_0}$ and $a_3 = \frac{1}{6}\frac{\partial^3 \phi(k)}{\partial k^3}\Big|_{k_0}$. Thus, these features can enable fast optimization algorithms.

Figure 3.7 shows an automatic dispersion compensation result. The fine retinal structure (Fig. 3.7A) is restored; this structure is significantly disturbed without dispersion compensation (Fig. 3.7B).

3.3 Motion correction

Although the SD-OCT has a high measurement speed and negligible distortion for cross-sectional imaging, 3D measurements of both the 3D structure and the time sequence of cross-sectional measurements require a total measurement time of a few seconds. Thus, motion correction is required. Two algorithms for axial motion correction–one for motion correction among the axial scans in a single cross section and the other for correction for each cross section–are described here.

3.3.1 Axial motion correction by Doppler shift

The Doppler shift in bulk motion causes artifacts in the flow images; they can be eliminated as mentioned in section 4.1. To eliminate these artifacts, the Doppler shifts of the bulk tissue motion at each axial scan are obtained. From these signals, the displacement of the tissue can also be estimated. Since the Doppler shift is caused by the movement of a sample along the optical axis, only the axial motion will be compensated. The axial velocity of the sample is expressed using the Doppler shift of bulk motion as follows:

$$v_{zi} = \frac{\lambda_0}{4n\pi T}\delta\phi_i^{bulk}, \tag{3.3}$$

where v_{zi} is the averaged axial velocity of the sample between the $(i-1)$-th and i-th axial scan; λ_0, the center wavelength; $\delta\phi_i^{bulk}$, the phase difference due to the axial bulk motion; and n, the refractive index of the tissue. Then, the relative axial displacement between the adjacent axial scans is calculated as

$$\delta z_i = v_{zi}T. \tag{3.4}$$

When the origin is set to the 0-th axial scan, the axial displacement for each axial scan is expressed as

$$\Delta z_i = \sum_{k=0}^{i} \delta z_k = \frac{\lambda_0}{4n\pi}\Delta\phi_i^{bulk}, \tag{3.5}$$

where $\Delta\phi_i^{bulk} = \sum_{k=0}^{i} \delta\phi_k^{bulk}$ is the phase differences corresponding to the mode value of histogram (Sec. 4.1) after phase unwrapping. In eq. (3.5), the change in the shape of the entire eye is not considered, such as the volume change due to the pressure of perfusion and accommodations. The OCT images are restored by shifting each axial scan along the depth by using Δz_i.

3.3.2 Correction by cross-correlation between neighboring frames

The lateral movement of retinal OCT images by head movements is quit small comparing to axial movement since volunteers are gazing a distant stationary target. The lateral displacement by the eye movement is estimated as ~ 40 μm from about 0.13 degree (standard deviation) of the gaze stability with head free and stationary fixation [52] and 17 mm of the distance between back nodal point to retina of the human eye [53]. It is comparable to the beam spot size on the retina (30 μm), even though the large saccadic eye movement occurs sometimes which cause significant large displacement. Thus, we use only the axial correlation for motion correction of 3D images. The axial shifts due to motion are estimated by the following one-dimensional cross correlation between the i-th axial scans in the $(j+1)$-th and j-th frames:

$$\chi_i(z') = \Gamma[I_{i,j+1}, I_{i,j}](z'), \tag{3.6}$$

where χ is the cross-correlation function, $\Gamma[]()$ is the cross-correlation operation, and $I_{i,j}(z)$ is the intensity profile of i-th axial scan in the j-th frame. The positions of the maximum peaks of each $\chi(z')$ denote the axial shifts. When a maximum correlation of $\chi_k(z')$ is smaller than the average of maximum correlations, i.e. $1/N \sum_{i=0}^{N-1} max[\chi_i(z')]$, $\chi_k(z')$ is discarded. The axial displacement between the j-th and $(j+1)$-th frames is determined as the median value of the maximum positions in each χ.

A displacement that includes the lateral shift between neighboring frames is simply determined by a two-dimensional cross correlation. The retina has a well-layered structure: therefore, the cross-correlation function between two retinal OCT images exhibits a fairly sharp peak along the axial direction. Motion correction in the axial direction works. In contrast, the shape of the cross-correlation function along the transversal direction is broadened. Motion correction in lateral direction depends on each case. When a characteristic landmark such as the ONH is present and imaging is performed over a large area, lateral motion correction can be applied; otherwise, it will not be effective. Further improvement is required in the lateral motion correction technique.

3.3.3 Performance of axial shift correction

Cross-sectional imaging with a large number of axial scans can be distorted by the sample motion. Figure 3.8 (A) shows a cross section of the human retina, which comprises 4000 axial scans. The acquisition time per image is 214 ms. Image distortion occurs due to sample motion at the region indicated by the black arrow. The axial displacement is compensated by using the motion correction algorithm for adjacent axial scans described in Sec. 3.3.1, as shown in Fig. 3.8 (B). This image is processed by flow imaging algorithms (Sec. 4.1). The bi-directional flow and the power of Doppler shift images are shown in Fig. 3.8 (C) and (D), respectively. Two small retinal vessels are evident. In the power of Doppler shift image, some choroidal vessels are observed. In the movie, the axial motion between each frame is compensated using the correlation-based method (section 3.3.2).

Figure 3.9 shows a comparison of the motion correction results for a 3D OCT volume set. Figure 3.9 (A) shows a fundus image produced from the OCT volume set by integration along depth, where the white arrows indicate the fast-scanning direction, and the red line indicates the location of the cross-sectional images shown in Fig. 3.9 (B), (C), and (D), which are without motion corrections, with the motion correction between neighboring frames, and with motion corrections between adjacent axial scans and between neighboring frames, respectively. The cross-sectional image along the slow-scanning direction shows significant axial displacement without any motion correction, as shown in Fig. 3.9 (B). The imaging time of this image is extremely longer than that of images along to fast-scanning direction; roughly several hundred times. Involuntary axial head movement cause large distortions. Since the head is not bound to stage and volunteers are trying to gaze a target, low frequency distortions maybe caused by small vibrations of muscles due

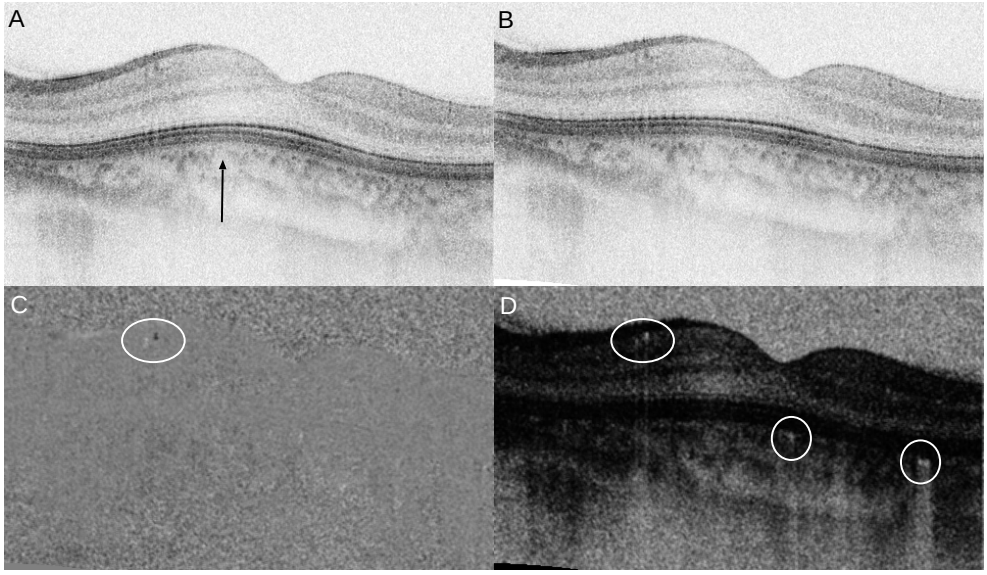

Figure 3.8: A sequence of OCT images and flow images of the human eye. Each image comprises 4000 axial scans and has a size of 5 mm $\times$ 1 mm (lateral $\times$ depth). The OCT images (A) without and (B) with the motion correction for adjacent axial scans are shown. The black arrow denotes the region in which axial image distortion has occurred. (C) Bi-directional flow and (D) the power of Doppler shift images show some vessels. Two retinal blood vessels appear in the bi-directional flow image (white circle). In the power of the Doppler shift image, the retinal vessels (upper white circle) and some choroidal vessels (two lower white circles) appear. Multimedia file is available on http://www.opticsexpress.org/abstract.cfm?id=97672

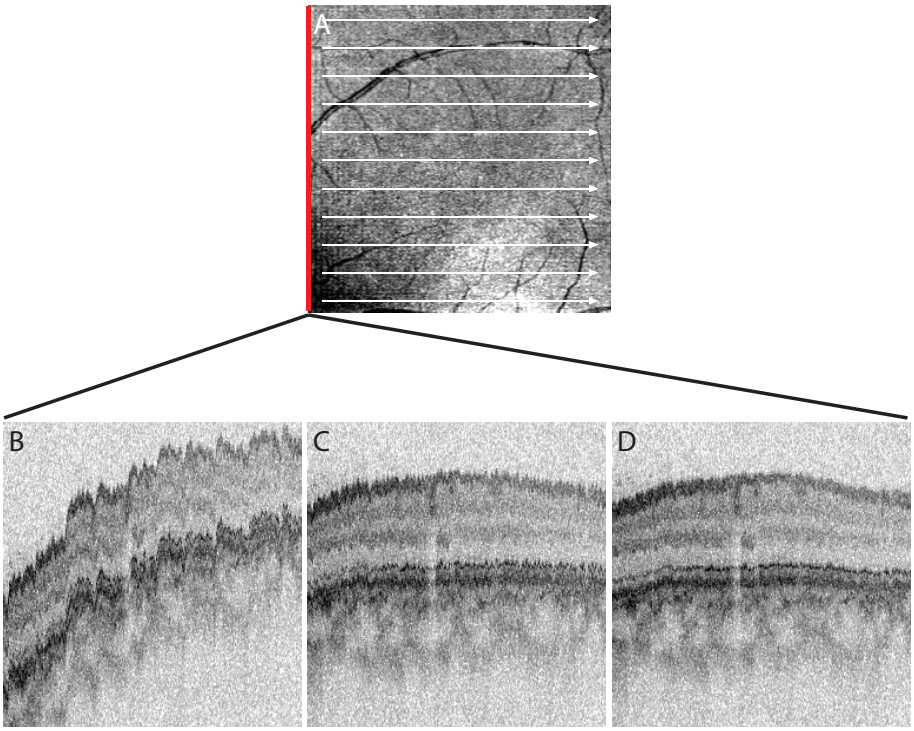

Figure 3.9: Comparison of the cross section of the 3D OCT volume along the slow-scanning direction. The fundus projection image (A) is produced from the 3D OCT volume set. White arrows represent the fast-scanning direction. The cross-sectional images (B) without motion correction, (C) with correction of the axial shift between neighboring frames, and (D) with correction of the axial shift between adjacent axial scans and neighboring frames corresponding to the red line in (A).

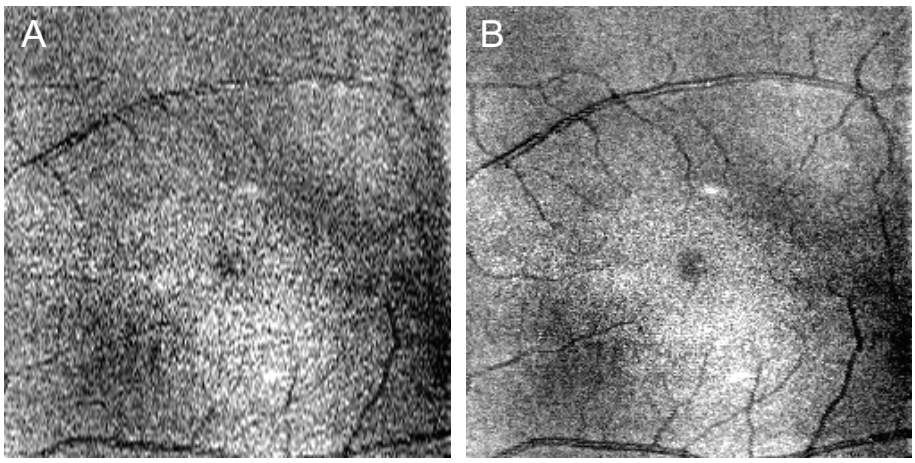

Figure 3.10: Fundus images of the human macula produced by (A) the preview mode and (B) integrating OCT signals. The imaging area size is 2.7 $\times$ 2.7 mm^2.

to tension. By axial motion correction between neighboring frames described in Sec. 3.3.2, the axial displacement is reduced; however, a small fluctuation remains due to the distortion of each image (Fig. 3.9 (C)). Although cross-sectional imaging with the conventional axial scan density does not exhibit an apparent distortion, some shearing does exist. This affects the performance of motion correction between neighboring frames. This distortion is improved by axial motion correction between adjacent axial scans, and a smoother structure is evident (Fig. 3.9 (D)). The mean values of normalized cross-correlation between neighboring frames are calculated for a 3D OCT volume set of the macular region, which comprises 1024 $\times$ 140 axial scans (5 mm $\times$ 5 mm). These are 0.25 without any motion correction, 0.33 with the motion correction between neighboring frames, and 0.38 with the motion corrections between adjacent axial scans and between neighboring frames. The increment of the normalized cross-correlation is + 0.08 $\pm$ 0.08 (mean $\pm$ standard deviation) through only the motion correction between neighboring frames and increased more (+ 0.05 $\pm$ 0.04) with the motion correction between adjacent axial scans.

3.4 Fast fundus preview

In the 3D measurement mode, a preview image of the fundus (fundus preview) is created immediately after acquisition. The algorithm is quite similar to that described in the literature (Ref. [54]). However, a simpler and faster method is used. The intensity map of the preview image $\mathscr{P}_{i,j}$ is obtained as follows:

$$\mathscr{P}_{i,j} = \log \left\{ \sum_{i=m}^{n} \left[I_{j,k}(k_i) - \frac{1}{N} \sum_{j=0}^{N-1} I_{j,k}(k_i) \right]^2 \right\}, \tag{3.7}$$

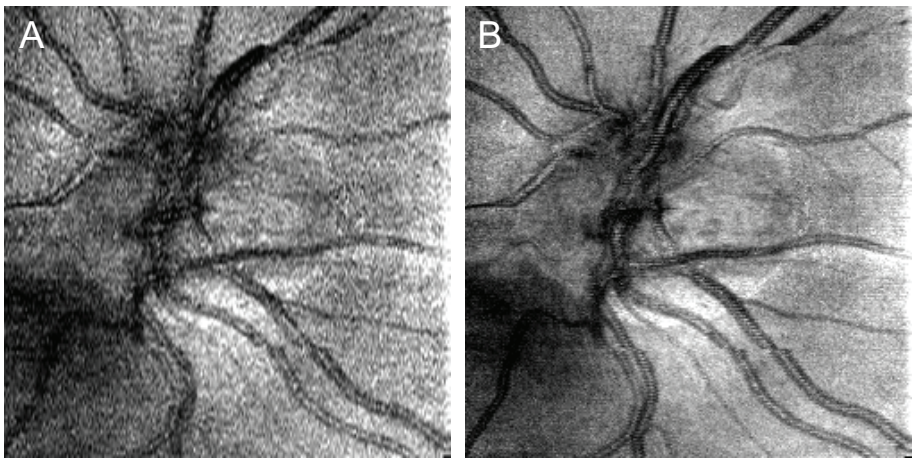

Figure 3.11: Fundus images of the ONH produced by (A) the preview mode and (B) integrating OCT signals. The imaging area is 2.7 $\times$ 2.7 mm^2.

where $I_{j,k}(k_i)$ denotes the raw spectra and j, k denote the indices of the horizontal and vertical positions, respectively. A portion $[I(k_m), I(k_n)]$ is extracted from a single spectral interference signal; then, an averaged spectrum calculated from N spectra, where N is the number of spectra in a single B-scan. Since the B-scan is performed along the horizontal direction, the spectra are averaged according to j. After subtracting the averaged spectra from each spectral fringe, the signal power is obtained by summation followed by squaring. This operation provides only the power of the interference signal because the non-interference offset of the spectrum has been omitted by subtracting the averaged spectrum. Then, the fundus projection image is revealed by log-compressed interference signal power.

This operation is applied to the spectral signals in the OCT volumes consisting of 250 $\times$ 250 axial scans and yields fundus preview images as shown in Fig. 3.10A and Fig. 3.11A (250 $\times$ 125 pixels, horizontal $\times$ vertical). The imaging quality of these images are comparable with that of the integrated fundus images obtained from 3D OCT data sets (Fig. 3.10B and Fig. 3.11B, 250 $\times$ 250 pixels). In these cases, only 256 pixels are extracted from the center of the 250 $\times$ 125 spectra (horizontal $\times$ vertical), where the line CCD camera has 2048 pixels and the original data sets have 250 $\times$ 250 spectra. Since the elaborate processes described in Sec. 3.1 are not required and small portions of the spectral interference signals are used, the total processing time with a PC (Athlon 64 3500+ processor and a 2 GB RAM) is small at $\sim$ 800 μs.

3.5 Retinal imaging

In order to verify the performance of high-speed ophthalmic SD-OCT, 3D imaging of the *in vivo* human retina is applied. The 3D volume rendered image of the

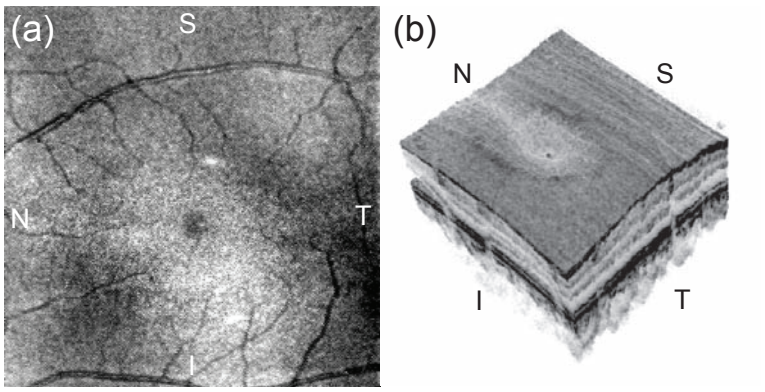

Figure 3.12: Three-dimensional image of the macula. (a) Fundus image created from 3D OCT volume set, (b) volume rendered image of 3D OCT image. S: superior, I: inferior, N: nasal, T: temporal. The imaging area size is 2.7 $\times$ 2.7 mm^2 (horizontal $\times$ vertical, 250 $\times$ 250 axial scans). The total imaging time for one volume set is 3.5 s.

macula and the ONH are shown in Fig. 3.12 and Fig. 3.13, respectively. The sample is the left eye of a 25-year-old Asian male. The total imaging time is 3.5 s with 250 $\times$ 256 axial scans. The inter-frame motion is corrected by using the correlation-based method (Sec. 3.3.2). The 3D structure of the human retina is observed. For visualizing the 3D image, a 3D visualization software called Amira (Mercury Computer Systems Inc., France) is used.

3.5.1 Imaging of retinal diseases

Here, some retinal diseases are imaged with the high-speed SD-OCT system in order to confirm the feasibility of the system for clinical use.

Age-related macular degeneration

Figure 3.14 shows several cross-sections of the AMD. The projection (Fig. 3.14 (a)) is created from the 3D OCT volume set; it shows the fundus-like image. In the superior part of the macula, there is an RPE detachment (the white arrow in Fig. 3.14 (b)). Retinal and RPE degeneration occurs at the central region of the macula, and several cysts appear (white arrows in Fig. 3.14 (c)). Since these images are created from the same OCT volume set, the positions of each cross-section can be referred. In Fig. 3.14 (a), three red lines show the locations of the cross-sections.

Macular hole

The second case is a macular hole (stage II). The high-quality cross-sectional image is shown in Fig. 3.15. The hole in the retina and several cysts around the

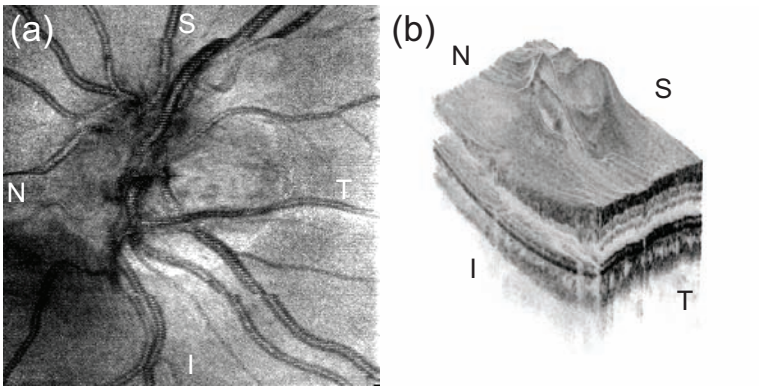

Figure 3.13: Three-dimensional image of the ONH. (a) Fundus image created from 3D OCT volume set, (b) volume rendered image of 3D OCT image. S:, superior, I: inferior, N: nasal, T: temporal. The imaging area size is 2.7 $\times$ 2.7 mm^2 (horizontal $\times$ vertical, 250 $\times$ 250 axial scans). The total imaging time for one volume set is 3.5 s.

hole are clearly observed. The operculum appear and is not completely detached. In addition, the detached vitreous cortex is evident. Figure 3.16 shows horizontal and virtual vertical scanning images and an virtual *en-face* slice, which are reconstructed from the 3D OCT volume set. From the two perpendicular cross-sections (Fig. 3.16 B and C), it is clear that the operculum is still connected at the inferior temporal edge of the hole. By *en-face* slicing the elevated retina, the honeycomb pattern of the cysts around the hole is observed (Fig. 3.16 D).

3.5.2 Discussions

Three-dimensional OCT imaging allows us to observe the arbitrarily cross-sectional image after image acquisition and compare OCT images to another clinical tools by image registration with fundus projection images. As a result, the retinal disease diagnosis will be improved.

3.6 Summary

The high-speed ophthalmic SD-OCT system has been developed and it is confirmed that this system can perform the high-speed imaging of the *in vivo* human retina. Furthermore, the 3D structure of retinal diseases is successfully obtained.

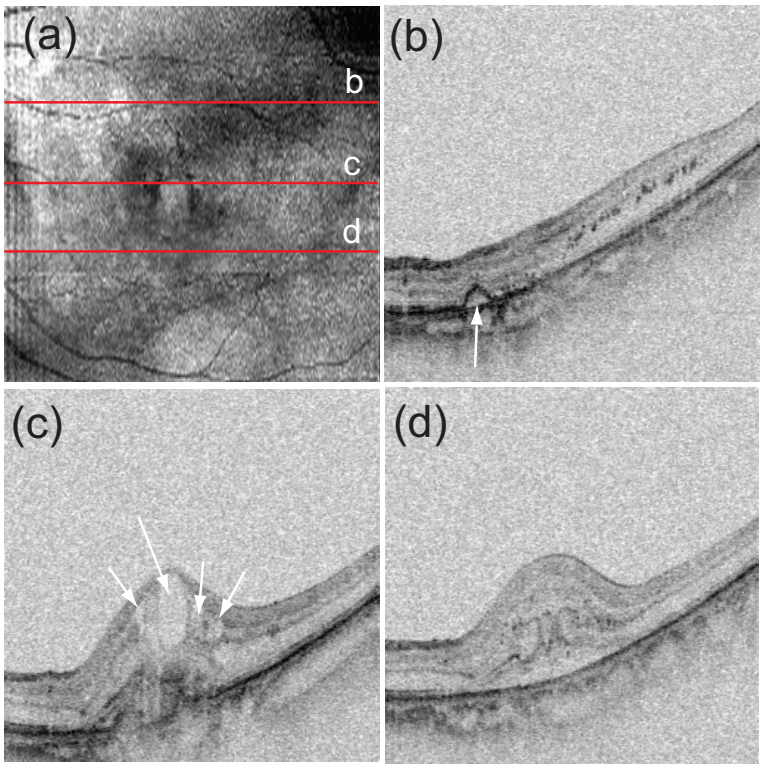

Figure 3.14: Three-dimensional imaging result for age-related macular degeneration (74-year-old Asian male, left eye). The imaging area size is 2.5 $\times$ 2.5 mm^2 (512 $\times$ 128) axial scans. (a) Fundus image created from the OCT volume set. (b),(c),(d) Cross-sectional images corresponding to the white lines in (a). In (b), the white arrow indicates RPE detachment. In (c), some macular cysts are shown (white arrows).

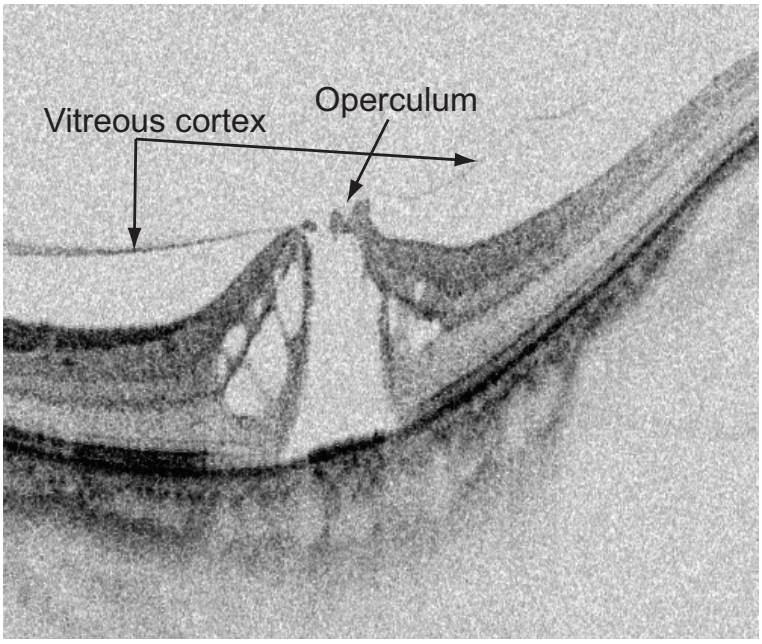

Figure 3.15: High definitive cross-section of a macular hole (70-year old Asian male, left eye). The imaging range is 2 mm $\times$ 5 mm (lateral $\times$ axial). The image consists of 2000 axial scans, and the imaging time is 107 ms.

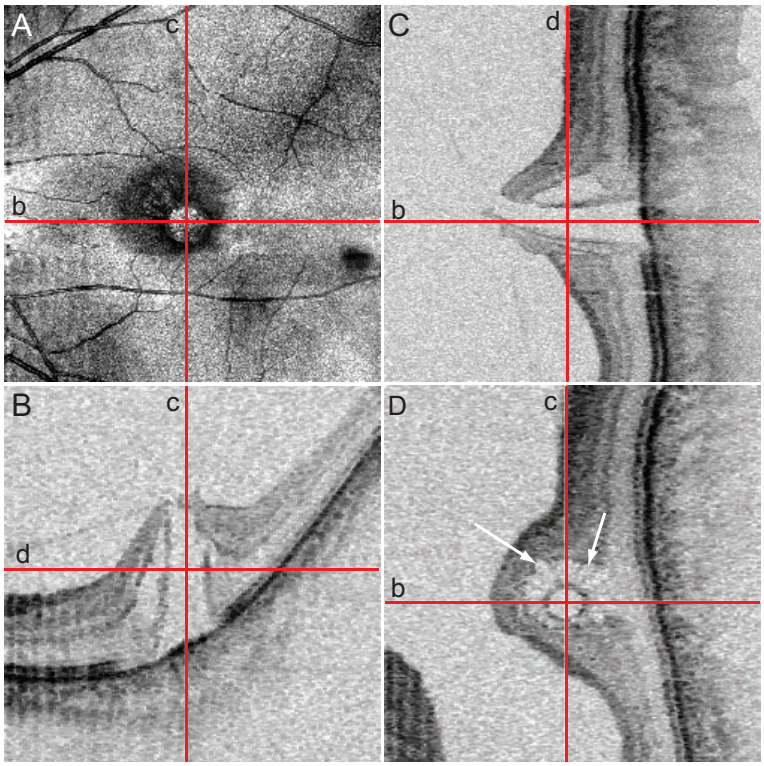

Figure 3.16: Three-dimensional imaging results for the macular hole patient. A: Fundus projection, B: horizontal scanning image, C: virtual vertical scanning image, and D: virtual *en-face* slice are shown. In the *en-face* slice (D), honeycomb pattern of cysts is appeared (white arrows).

Chapter 4

Optical coherence angiography — vessel imaging by SD-OCT*

Ocular circulation is very important not only for ophthalmic diagnosis but also for the study of eye diseases such as glaucoma [55], diabetic retinopathy [56], and age-related macular degeneration [57]. Fluorescein angiography (FA) and indocyanine green angiography (ICGA) [58] are the chief diagnostic methods for retinal diseases. Ocular vessels are contrasted by using the fluorescence of the dyes injected into a vein. Since the excitation wavelength of indocyanine green is relatively longer than that of sodium fluorescein, the choroidal vasculature is clearly visualized in ICGA rather than FA. However, these methods are invasive. The skin will be colored in yellow by the fluorescein dye. Intravenous administrations of sodium fluorescein and indocyanine green are considered as safe procedures but not no risk. There are some adverse effects due to dye injection. A frequencies of mild adverse effects, such as nausea, vomiting, and so forth, are between less than 1 % and 10 % for FA [59] and 0.15 % for ICGA [60]. Although rare, some severe adverse effects such as anaphylaxis also occur.

There are several noninvasive blood flow assessment techniques that use lasers, which have been applied in several investigations of ocular circulation [61]. Laser Doppler velocimetry (LDV) measures the blood flow velocity, and it has been applied to human retinal vessels [62; 63]. Microcirculation in the optic nerve head (ONH) [64] and the choroidal blood flow [65] of the human eye have been investigated by laser Doppler flowmetry (LDF) [66], which acquires the volume, flux, and average velocity of the red blood cells in the small vessels surrounded by the scattering tissues. Two-dimensional perfusion mapping of blood flow can be obtained by using scanning laser Doppler flowmetry (SLDF) [67; 68], laser speckle photography [69], and laser speckle flowgraphy [70]. Although these techniques

*The portions of this chapter have been published in the following article:
S. Makita, Y. Hong, M. Yamanari, T. Yatagai and Y. Yasuno, "Optical coherence angiography," Optics Express **14**, 7821-7840, (2006). http://www.opticsexpress.org/abstract.cfm?id=97672

are useful for investigating the ocular circulation, they demonstrate no or poor ability to resolve the depth structure. SLDF, which is based on scanning laser ophthalmoscopy, exhibit depth-resolving power inherently due to the confocal effect; however, its axial resolution is limited to $\sim$ 300 μm due to pupil size and eye aberrations.

Optical Doppler tomography (ODT) [71] has been applied to the depth-resolved cross-sectional flow imaging of *in vivo* tissues [12; 13; 14; 72; 73]. Further, ODT has been demonstrated for blood flow imaging of retinal vessels [74; 75]. These ODTs are based on time-domain optical coherence tomography (OCT) [1] – a cross-sectional imaging technique with high spatial resolution. Three-dimensional vessel structure extraction is possible using 3D scanning [76]. Three-dimensional retinal imaging is, however, restricted by a substantial and frequent head movement and exposure limit for the eye. Short imaging time is required to suppress the influence of the head movement, but the scanning speed of OCT is restricted to maintain sustainable sensitivity with low power of probing beam. In recent years, spectral-domain OCT (SD-OCT), which has a higher sensitivity than time-domain OCT [21; 22; 23], has emerged. SD-OCT has been performed at a 150 fold faster measurement speed than time-domain OCT [24]. This technique allows high-resolution and highly accurate 3D *in vivo* structural measurement of the human retina [77; 78]. High-speed retinal blood flow imaging by using SD-OCT has been demonstrated [79; 80; 81].

We present an *in vivo* noninvasive angiography of the human retina. Three-dimensional retinal imaging is performed by using high-speed SD-OCT. The bulk motion artifacts in the flow images are compensated by a histogram-based algorithm. The axial eye movements during 3D imaging are compensated by using Doppler shifts of the bulk motion for axial displacement between adjacent axial scans and a simple and fast correlation-based algorithm for axial shifts between neighboring images. Three-dimensional retinal and choroidal vasculature are visualized, and two-dimensional vessel imaging that is comparable to FA and ICGA are demonstrated.

4.1 Blood flow imaging by SD-OCT

In our method, the Doppler shift of the OCT signal is utilized to contrast the blood vessels. To achieve the flow images, first, the bulk motion artifacts are eliminated by a histogram-based algorithm. Then, two flow imaging implementations, bi-directional flow and power of Doppler shift, are applied. Finally, these two images are averaged using a moving average filter.

A bi-directional flow image f_i is obtained by using the phase difference between adjacent axial scans $\Delta\phi_i$ [12] as follows:

$$f_i(z) = \frac{\Delta\phi_i(z)}{2\pi T}. \tag{4.1}$$

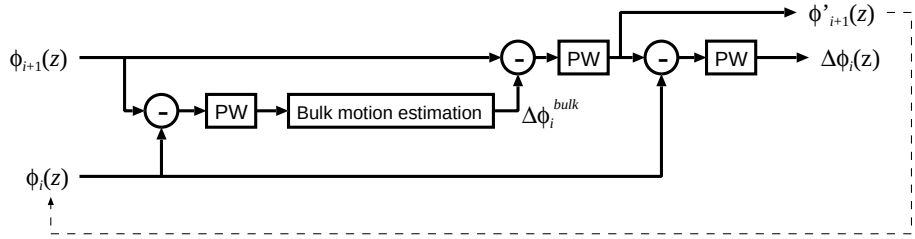

Figure 4.1: The diagram of the bulk motion artifact elimination algorithm. $\phi_i(z), \phi_i'(z)$: phases of i-th axial scan before elimination and after elimination, respectively, $\Delta\phi_i(z)$: phase differences, $\Delta\phi_i^{bulk}$: the phase difference corresponding to the phase shift from 0-th axial scan due to the bulk motion of the sample. PW: phase wrapping process.

Here, T denotes the axial scan period and $i \in [0, N)$ denotes the number of axial scan. By using the axial scan period, the maximum detectable Doppler shift is estimated as f_{max} = $\pm$ 1/2T. In our system, this value is calculated to be $\pm$ 9.38 kHz. Further, the minimum detectable Doppler shift is defined on the basis of the fluctuation of the phase difference. As mentioned by Park $et.al$, the minimum detectable Doppler shift depends on the signal-to-noise ratio and the ratio of the spacing of transversal scanning to the beam spot size [82].

Another implementation, which is power of Doppler shift imaging, is also applied [82]. The power of the Doppler shift image σ_i^2 is obtained as

$$\sigma_i^2(z) = \Delta\phi_i^2(z), \tag{4.2}$$

and it exhibits similar properties to Doppler standard deviation imaging [13].

4.1.1 Elimination of motion artifacts

During retinal imaging, significant involuntary head movements cause large artifacts in the flow images. To eliminate these bulk motion-induced artifacts, we use a histogram-based bulk motion estimation method [83; 15] and phase wrapping method [80]. The diagram of the algorithm is shown in Fig. 4.1. The phases of adjacent axial scans $\phi_i(z), \phi_{i+1}(z)$ are subtracted ($\phi_{i+1}(z) - \phi_i(z)$) and wrapped into -$\pi$ to π. From the differences, the phase difference $\Delta\phi_i^{bulk}$ corresponding to the bulk motion is obtained by the histogram-based bulk motion artifact elimination method. $\Delta\phi_i^{bulk}$ is subtracted from the raw phases of the axial scan that follow $\phi_{i+1}(z)$; then, phases are wrapped. Then, the phase difference $\Delta\phi_i(z)$ is obtained by subtracting $\phi_i(z)$ from the compensated phase $\phi_{i+1}'(z)$ and phase wrapping. $\phi_{i+1}'(z)$ is used for the elimination of next axial scan.

When the vessel region is smaller than the other tissue region or the blood flow distribution exhibits a wide velocity range, the phase difference corresponding to the Doppler shift frequency due to the bulk motion will be the maximum count

in the histogram of the phase differences between two adjacent axial scans. In other words, the Doppler shift of bulk motion is estimated by using the mode of the phase differences. Yang et al. determined the number of histogram bins from the phase stability [15]. However, the histogram shape also depends on the number of samples. If the number of samples is small, the histogram bin width will be relatively small, resulting in a noisy histogram. We apply the following data-based histogram bin width determination rule, which is known as the Freedman & Diaconis rule [84]:

$$h = 2IQm^{-1/3}, \tag{4.3}$$

where h denotes the histogram bin width;, IQ, the interquartile range; and m, the number of samples. Prior to the formulation of histograms, the noise regions are eliminated by using an intensity-based thresholding. The threshold level is determined from the mean values of the noise floor in the OCT images.

Although a smooth histogram can be obtained by using a large histogram bin width, another problem exists. Since the histogram bin width increases, the accuracy of the bulk motion calculation decreases. In order to increase the accuracy of measurement of the bulk motion Doppler shifts, we average several histograms with different origins of bins; the resulting histogram is referred to as an averaged shifted histogram [85].

The histograms of one depth profile of the phase differences in the region lacking vessels are shown in Fig. 4.2. The histogram in which the number of bins is determined by the phase-noise-based rule shows an almost zero-mean probability distribution (Fig. 4.2 (a)). Here, we estimate the phase noise by using the lateral spacing and beam spot size [82]. However, the maximum count is observed at approximately 1 radian. This error might be due to the extremely narrow histogram bin width. By using the Freedman & Diaconis rule (Fig. 4.2 (b)), such types of error peaks disappear. Instead, the histogram bin widths broaden. The accuracy of the bulk motion Doppler shift measurements decreases. By averaging the eight histograms with different origin of bins and identical histogram bin width as determined by the Freedman & Diaconis rule, a very smooth phase difference distribution is obtained, as shown in Fig. 4.2 (c). For comparison, Fig. 4.2 (d) shows the histogram with a bin width that is one-eighth that of one of the result shown in Fig. 4.2 (b). This histogram is extremely noisy, and the error in the maximum count is observed at approximately 1 radian.

Figure 4.3 shows flow images of the retinal vessels near the ONH with bulk motion artifact elimination by using different histogram bin width determination methods. Bi-directional flow images are obtained after bulk motion artifact elimination, differentiation of phase, and 19 $\times$ 3 pixels (29 μm in the lateral direction $\times$ 10 μm in the axial direction) averaging filtering. In Fig. 4.3 (A) (phase-noise-based method), bulk motion artifacts remain in the upper part of the blood vessels, which is indicated by the white arrow. These artifacts are suppressed in Fig. 4.3 (B) (simple Freedman & Diaconis rule), but the other artifact (yellow arrow) is enhanced. They disappear in Fig. 4.3 (C) (averaged shifted histogram). The elimi-

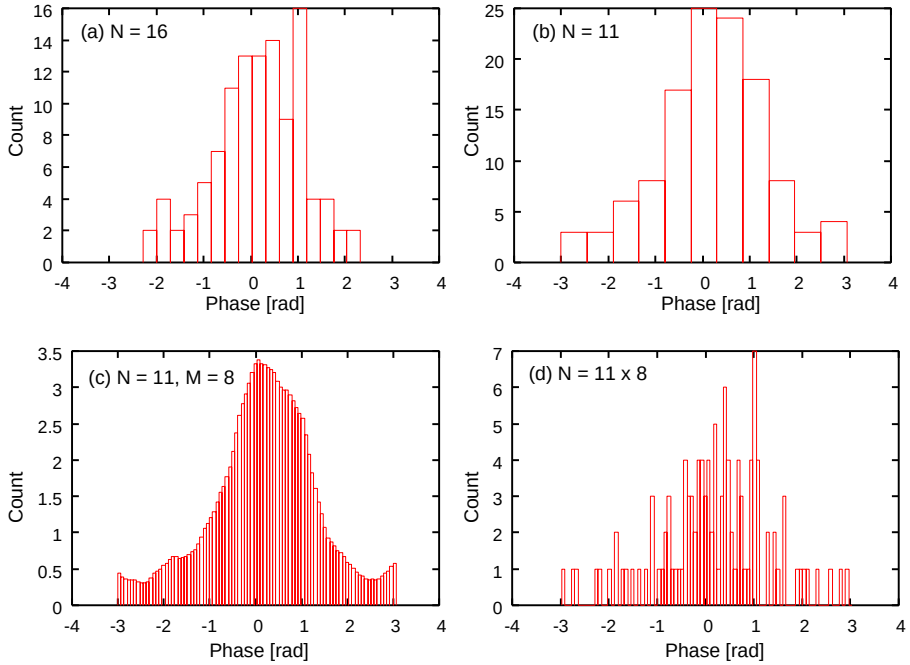

Figure 4.2: Comparison of histograms with different number of histogram bins. N: number of histogram bins, M: the number of histograms used in the averaging process. The histogram bin width of each histogram is determined by (a) the phase noise and (b), (c) the Freedman & Diaconis rule. (c) is the averaged shifted histogram using eight histograms. (d) is a conventional histogram with a histogram bin width equivalent to that of the histogram in (c).

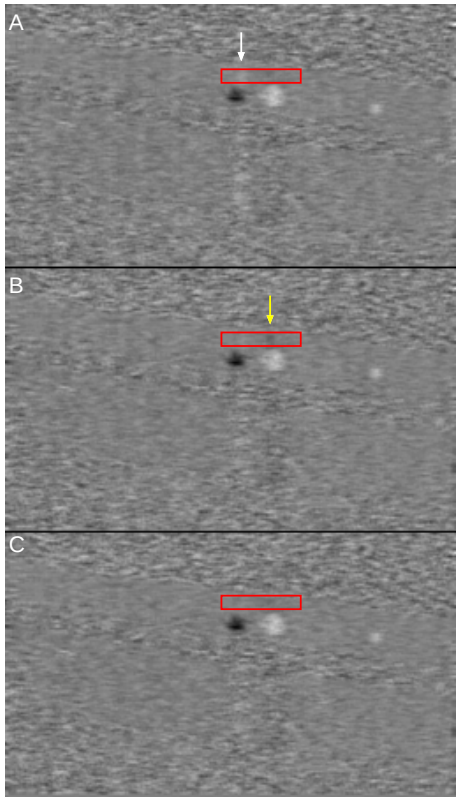

Figure 4.3: Comparison of the blood flow images after bulk motion elimination using different histogram bin width determination methods. Phase-noise-based method (A) and the Freedman & Diaconis rule (B), (C) are used to determine the histogram bin width. An averaged shifted histogram is used for (C). The white and yellow arrows indicate the bulk motion artifacts due to the estimation error. The images consist of 1024 axial scans and cover 1.5 mm in the transversal direction. The black and white colors denote Doppler shifts of -5.6 and +5.6 kHz, respectively.

nation errors are calculated as discrepancy of phases from zero radian at above the blood vessels.The RMS errors from zero radian, in the red boxes, are 0.150, 0.139, and 0.113 radians for Fig. 4.3 (A), (B), and (C), respectively.

4.2 OCA for the human eye

Three-dimensional volume sets of the flow images are used to generate 3D vasculature images and en-face vessel images. To eliminate the noise in the regions with no signal, only the areas of interest are extracted, i.e., from the vitreoretinal interface to the deepest penetration points, where signals are equal to noise floor. Two boundaries of the ares are segmented in the OCT images. Furthermore, a high reflectivity layer – corresponding to the inner/outer segment boundary (IS/OS), retinal pigment epithelium (RPE), and choriocapillaris (CC) – is segmented in order to separate the retinal and choroidal layers. The OCT signals exhibit low intensities in some retinal vessels since the high blood flow velocity in the vessel results in a fringe washout.

The anterior boundary of the ares of interest is determined using an algorithm similar to that presented by Mujat *et al.* [86]. In order to suppress noise, the OCT images are blurred by using a Gaussian filter with a standard deviation of 3×3 pixels; gradient magnitude images are thus obtained. These images are indicated with the sign of the axial gradient to distinguish whether anterior edge or posterior edge.The thresholding of the gradient magnitude images yields binary edge images. The threshold level is determined from the statistical properties of noise to maintain the interfaces as a continuous curve. After eliminating the small particles in the binary edge images, the first exceeding points over the threshold level from the top of the images are detected. Then, positions that have a maximum gradient within ten pixels lower than the first unity points are obtained. In order to smooth the curve, an iterative smoothing algorithm is used. The large second derivative of axial positions of boundary are ignored, and then, a linear interpolation of the boundary positions is performed. These steps are applied until the curve is significantly smooth. Then, a median filter with a rank of 15 is applied.

The high reflectivity layer is segmented prior to posterior boundary segmentation to determine the retinal vessel regions. The axial positions of the maximum gradient lower than 25 pixels from the anterior boundary are detected. Some axial scans with no edges are ignored. The intensities of 15 pixels around the detected positions along the axial direction are averaged. Then, they are smoothed using a Savitzky-Golay filter. The points at which the intensity before smoothing significantly drops from the smoothed results are considered to form the vessel region. The signals under the blood vessels are weak due to the absorption of blood. Both the vessel regions and the no-edge regions are expanded by 10 pixels on both sides to completely eliminate the regions. The positions of the high reflectivity layer of both regions are then obtained by linear interpolation. The positions of this layer are smoothed in a similar manner as the segmentation of the anterior boundary.

For the posterior boundary segmentation, the boundaries between the signals and noises are determined. Binary images are created by thresholding for the Gaussian blurred intensity images. The threshold level is determined by using a histogram of logarithmic intensity. The probability density of noise exhibits a sharp peak; therefore, the threshold level is set to a value which exhibits a count of a fifth part of the maximum count in the histogram. Then, the small particles are eliminated. The threshold of the particle size is determined by the image size. The first unity points from the posterior edge of the images are detected. The posterior boundary curve is interpolated at no-edge and vessel regions. Then, the curve is smoothed using the same method to that is performed for the anterior boundary and high reflectivity layer.

All the segmentation parameters are automatically determined. By using a PC (Athlon 64 3500+ processor and a 2 GB RAM), the processing, which includes flow imaging, motion corrections (Sec. 3.3), and segmentations, takes approximately 11.5 seconds per frame that comprises 1024 axial scans.

The 3D vasculature is imaged by a volume rendering of the segmented volumes. The bi-directional flow images are squared to achieve a high dynamic range for visualizing the vasculature. For both the 3D bi-directional and the power of Doppler shift volume sets, 3D Gaussian filtering is performed to suppress the spurious noise and discontinuities in the vasculature.

Two-dimensional angiograms are produced by integrating the flow volume sets along the axial direction. Since the power of the Doppler shift images have a higher sensitivity than the bi-directional flow images, angiograms produced from the former exhibit a higher contrast. Furthermore, the retinal vessels can be separated from the choroidal vessels by segmenting the high reflectivity layer. Two angiograms of the retinal and choroidal vessels can be produced individually, which might correspond to FA and ICGA.

4.3 Results

4.3.1 Three-dimensional vasculature imaging

In vivo 3D blood flow imaging has been performed in a healthy human eye. The macular region of the retina is imaged with 1024 axial scans in one frame and 140 frames acquired over an area of 5 mm $\times$ 5 mm. The resulting images are shown in Fig. 4.4. Figure 4.4 (A) shows the fundus projection image of the OCT volume set. Three boundaries segmented by using the algorithm that is described in Sec. 4.2 are indicated in the sequence of OCT images. In the bi-directional flow image (Fig. 4.4 (C)), the blood flow from some retinal vessels is observed. However, the flow in some vessels and the choroidal vessels is not visible. In contrast, the power of Doppler shift image (Fig. 4.4 (D)) clearly shows the flow in the retinal vessels and some choroidal vessels. However, artifacts are observed in the low signal regions (i.e., vitreous, outer nuclear layer, and deeper region than penetration). Artifacts also appear under the blood vessels due to the absorption of blood and

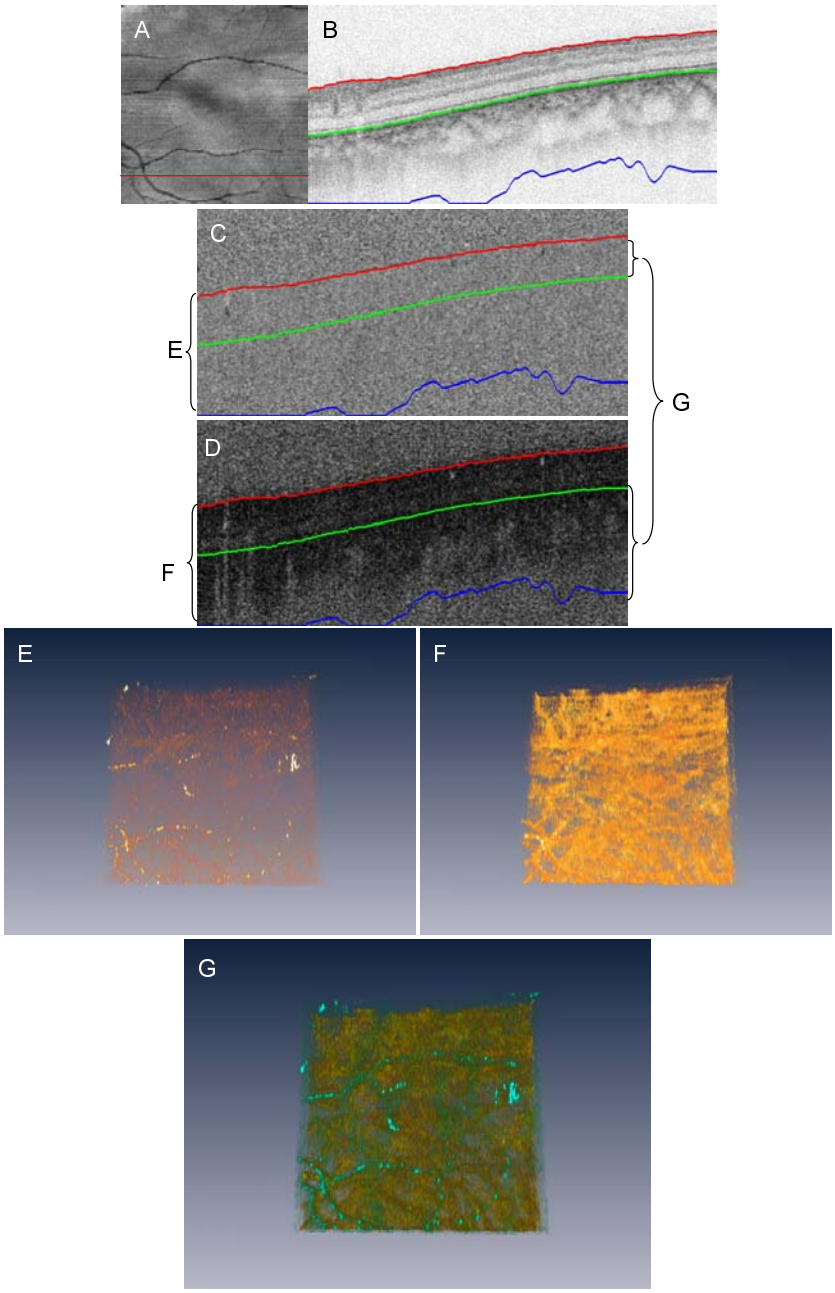

Figure 4.4: Three-dimensional optical coherence angiography of the macular region. The fundus projection image of the 3D OCT volume set (A) and the sequence of the OCT images (B) are shown. The segmented anterior (red) and posterior (blue) boundaries of the tissue and the high reflectivity layer (green) are indicated in the OCT images (B). The volume rendering images (E) and (F) are produced from stacks of bi-directional flow images (C) and the power of Doppler shift images (D). The composite volume rendering image (G) is a combination of the retinal part of (E) (encoded in cyan) and the choroidal part of (F) (encoded in yellow). The image size is 5 mm $\times$ 5 mm, corresponding to 1024 $\times$ 138 axial scans. Multimedia files are available on http://www.opticsexpress.org/abstract.cfm?id=97672

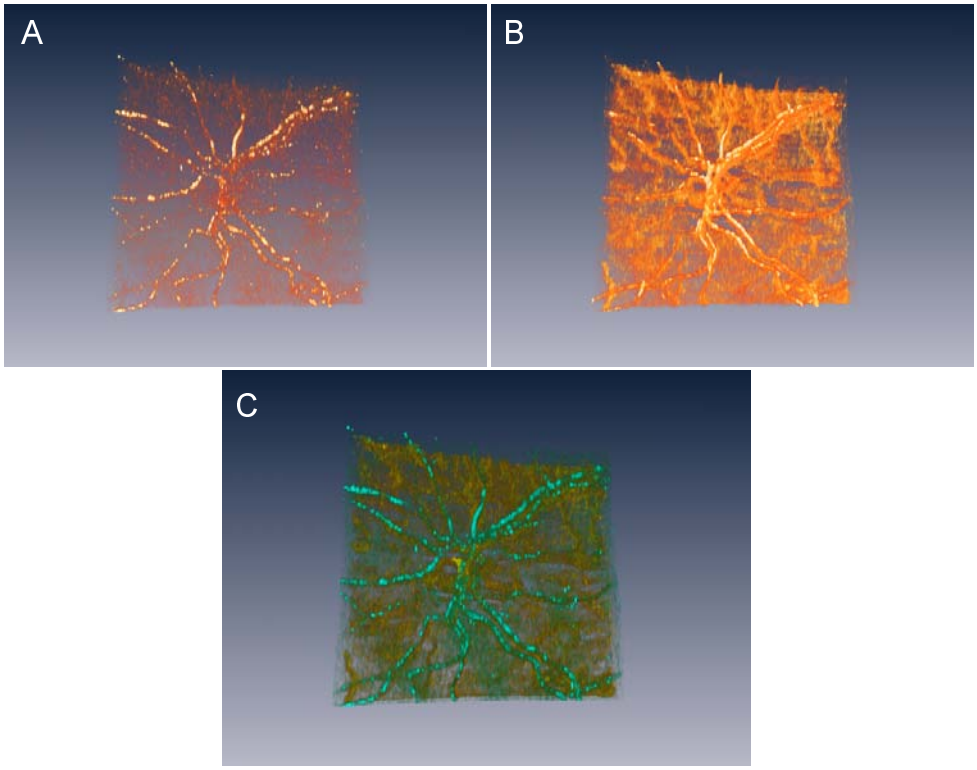

Figure 4.5: Three-dimensional optical coherence angiography of the ONH. (A): volume rendering image of the bi-directional flow volume set (upper left), (B): volume rendering image of the power of Doppler shift volume set, (C): the composite volume rendering image of the retinal part of (A) (cyan) and the choroidal part of (B) (yellow). The image size is 5 mm $\times$ 5 mm, corresponding to 1024 $\times$ 138 axial scans. Multimedia files are available on http://www.opticsexpress.org/abstract.cfm?id=97672

forward scattering by the red blood cells. Three-dimensional ocular vasculature is presented using volume rendering images of both the squared bi-directional flow and the power of Doppler shift volume sets. These are volume rendered after 3D Gaussian filtering with a standard deviation of $1 \times 1.5 \times 1$ pixels (axial direction $\times$ B-scanning direction $\times$ C-scanning direction). The volume rendering image of the squared bi-directional flow volume (Fig. 4.4 (E)) shows the vasculature of the retinal vessels; however, the choroidal vessels are not clearly observed. Artifact are observed at the surface that have high specular reflection. Although artifacts are observed under the retinal vessels due to the shadowing effect, and substantial noise occurs at the outer nuclear layer, the volume rendering image of the power of Doppler shift volume set (Fig. 4.4 (F)) shows the retinal vasculature and choroidal vessels.

The retinal and choroidal layers can be separated at the high reflectivity layer corresponding to IS/OS, RPE, and CC. A combination of the retinal part from Fig. 4.4 (E) and the choroidal part from Fig. 4.4 (F) is shown in Fig. 4.4 (G). The anterior part is encoded in cyan and the posterior part, yellow. Since the 3D squared bi-directional flow images exhibit low noise and small artifacts and the 3D power of Doppler shift images exhibit choroidal vessels, this combination results in a better visualization. Three-dimensional volume rendering images of the ONH region are shown in Fig. 4.5 and its movies.

4.3.2 *En face* vasculature imaging

Although the power of Doppler shift images exhibit some artifacts, they are highly sensitive. The projection of the power of Doppler shift volume set serves as two-dimensional angiography. In this case, the artifacts under the vessels enhance the contrast of the projection images. Two-dimensional angiographies for both the macular and ONH regions are shown in Figs. 4.6 and 4.7, respectively.

The projection images with the entire depth integration of the power of Doppler shift volume sets are shown in Figs. 4.6 (A) (macula) and 4.7 (A) (ONH). By selecting the integration range as the tissue region, the contrast of the images is slightly enhanced, as shown in Figs. 4.6 (C) and 4.7 (C). Only retinal vessels are visible in the projection images of the retinal layer (Figs. 4.6 (D) and 4.7 (D)). On the other hand, the projection images of the choroidal part reveal not only the choroidal vessels but also the retinal vessels due to shadowing effect (Figs. 4.6 (E) and 4.7 (E)). For practical applications, composite false-colored images are created from these projection image sets to distinguish the retinal vessels and the choroidal vessels. For the colored images, each of the three layers – red, green, and blue – are produced by the following manner. The images of the retina and the choroid are normalized; they correspond to the blue and green channels, respectively. The retinal images are inverted and multiplied with the images of the choroid in order to suppress the retinal vessel artifacts; this is the yellow channel. This process renders the retinal and choroidal vessels cyan and yellow, respectively (Figs. 4.6 (F) and 4.7 (F)).

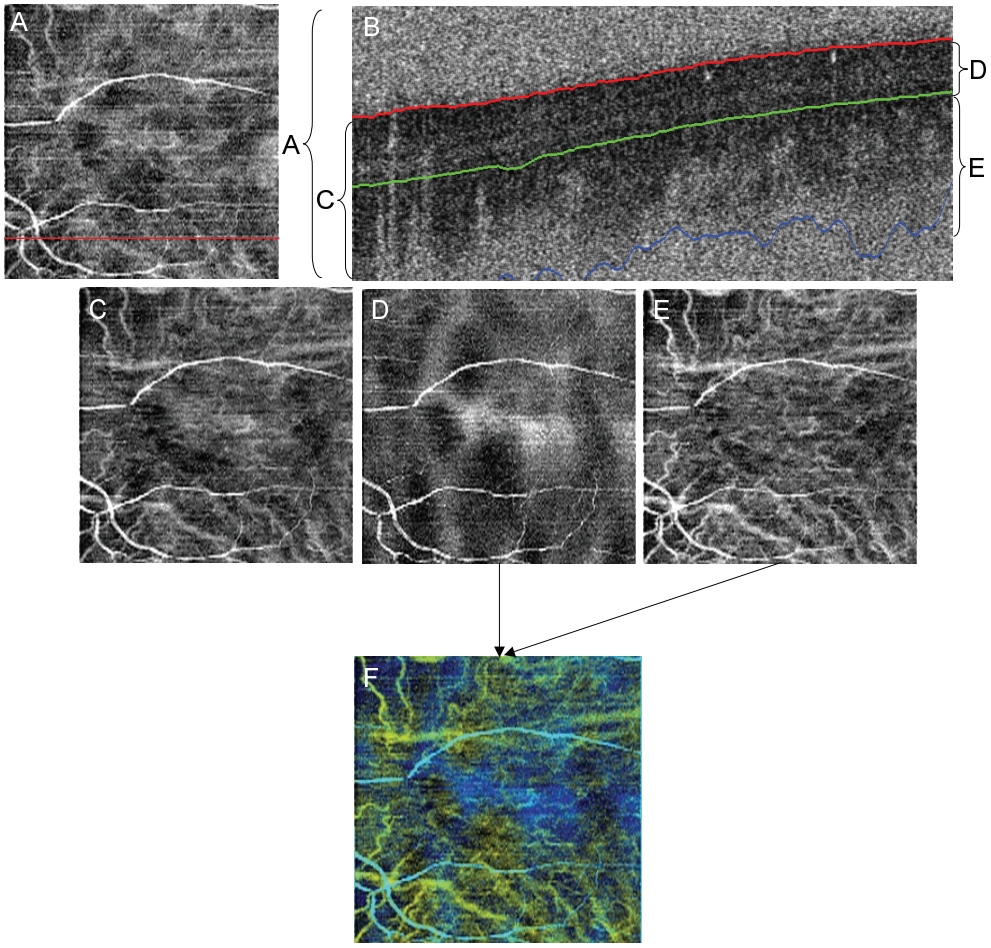

Figure 4.6: Optical coherence angiography of the macula lutea of the human eye. Each image is produced by the integration of (A) the entire depth, (C) tissue region, (D) retinal part, and (E) choroidal part of the power of Doppler shift images. (F) is a combination of (D) and (E). In the cross-sectional flow image (B), each integration range is indicated.

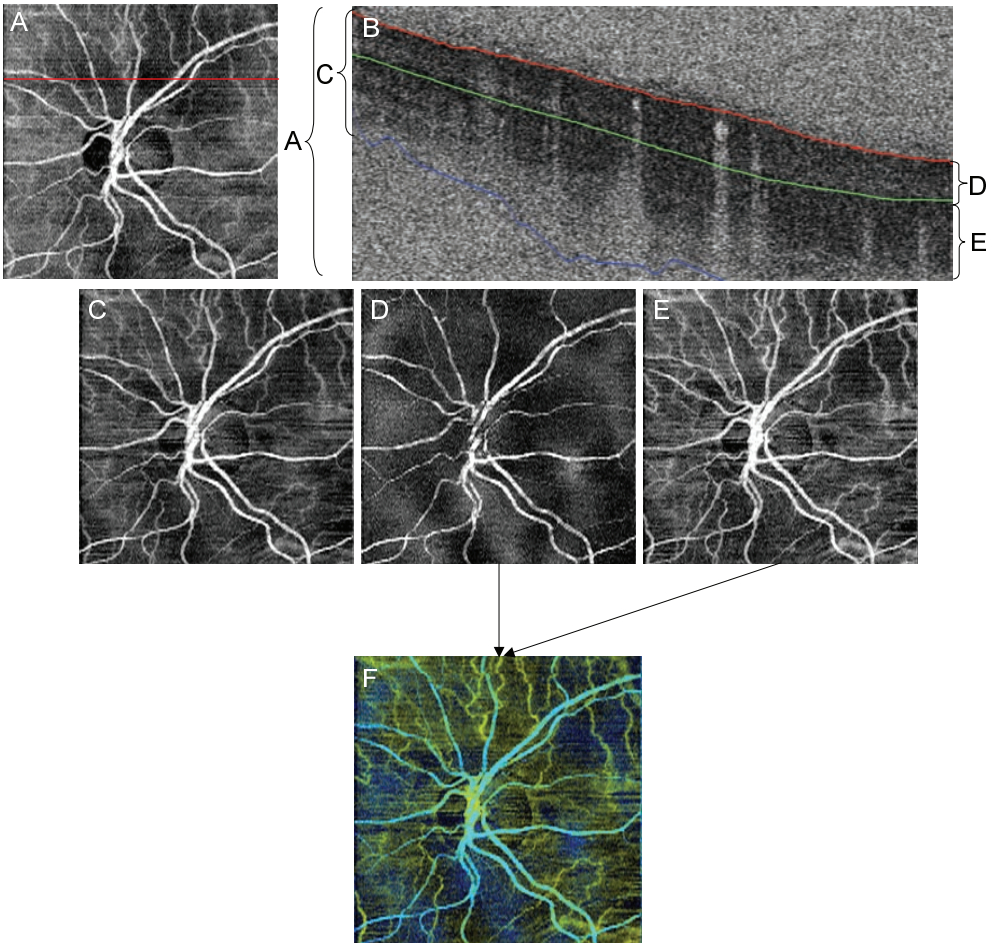

Figure 4.7: Optical coherence angiography of the ONH of the human eye. Each image is produced by the integration of (A) the entire depth, (C) tissue region, (D) retinal part, and (E) choroidal part of the power of Doppler shift images. And (F) is a combination of (D) and (E). In the cross-sectional flow image (B), each integration range is indicated.

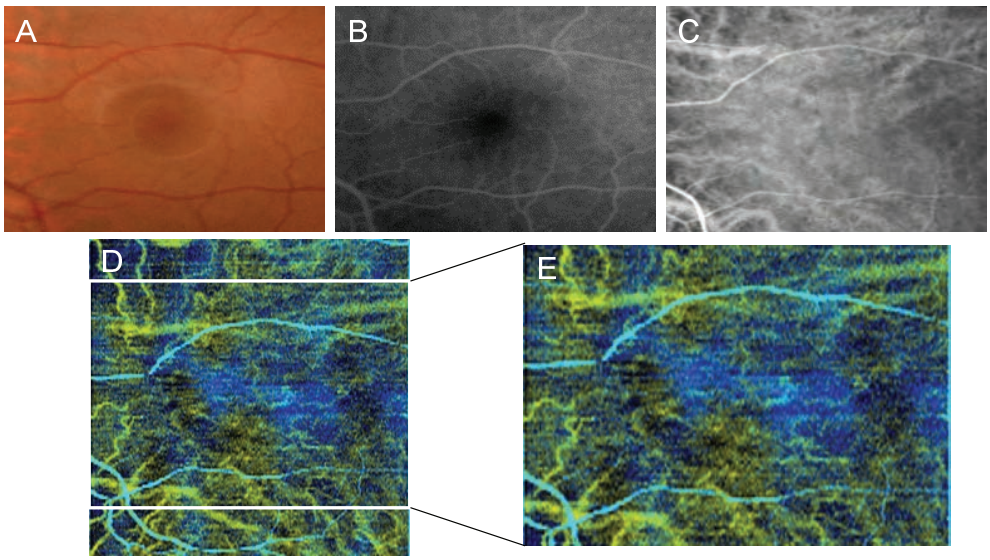

Figure 4.8: Comparison of the angiographies of the macula lutea. From the left-hand side, the images of the fundus photography (A), FA (B), and ICGA (C) are shown. Two-dimensional OCA image (D) is cropped to compare it with to the other angiographies (E). The retinal vessels and some choroidal vessels appear in (D), which is in agreement with FA (B) and ICGA (C). The size of the image (E) is 5 mm $\times$ 3.6 mm (horizontal $\times$ vertical).

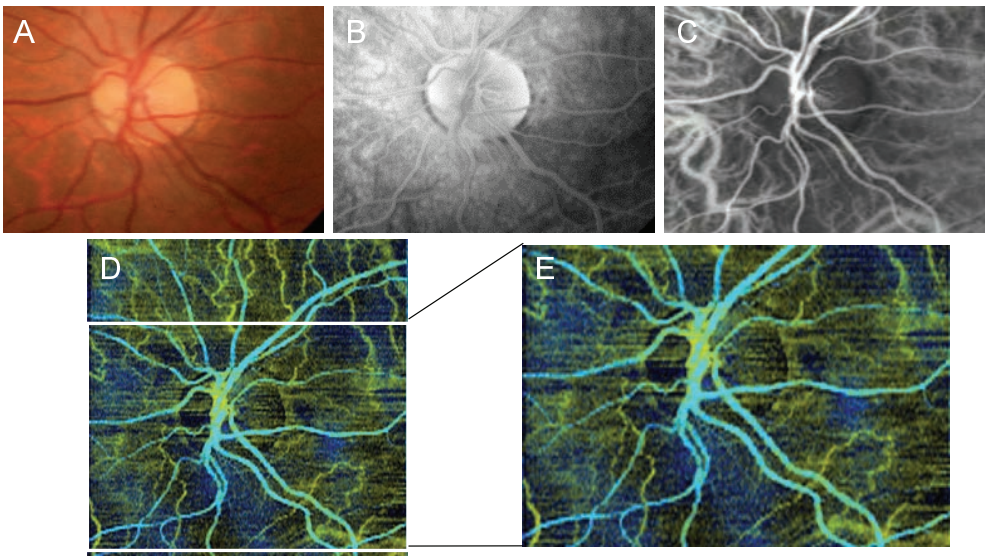

Figure 4.9: Comparison of the angiographies of the ONH. From the left-hand side, the images of the fundus photography (A), FA (B), and ICGA (C) are shown. Two-dimensional OCA image (D) is cropped to compare it with the other angiographies (E). The retinal vessels and some choroidal vessels appear in (D), which is in agreement with FA (B) and ICGA (C). The size of the image (E) is 5 mm $\times$ 3.6 mm (horizontal $\times$ vertical).

Since there are no retinal and choroidal layers in the optic disk, the segmentation of the high reflectivity layer at the optic disk is inappropriate. However, the high reflectivity layer segmentation algorithm behaves to detect the posterior boundary of retinal vessels, so that the retinal vessels are included into the retinal part. Since the almost of all OCT signals in the retinal vessels at the optic disk are disappeared due to fringe washout, large rising edges at the posterior boundary of the retinal vessels are detected. Nevertheless, the discontinuity of the retinal vessel inside the optic disk is observed in Fig. 4.7 (B). Further improvement of the segmentation algorithm is required.

Figure 4.8 shows a comparison between FA, ICGA, and two-dimensional OCA of the macular region. The angiograms of the ONH are also shown in Fig. 4.9. Intravenous injection has been administrated with sodium fluorescein (2.5 ml of 10 percent solution) and indocyanine green (2 ml of 1.25 percent solution). Each fluorescence angiograms are acquired at 2 minutes 43 seconds (Fig. 4.8 (B)), 14 minutes 56 seconds (Fig. 4.9 (B)), 27 seconds (Fig. 4.8 (C)), and 45 seconds (Fig. 4.9 (C)) after dye injection. Both the two-dimensional OCA images of the macular region and the ONH shows the vasculature of the retinal vessels and choroidal vessels. Fine retinal vessels in the macular region are visible with FA, but not with OCA. It is expected that the density of the axial scan is not sufficient for detecting these small vessels and/or their blood flow velocity is low. Some thick choroidal vessels that appear in ICGA do not appear in the OCA images. The reasons for this are assumed to be their low blood flow velocity and/or the low backscattered light from these vessels. However, these OCA images are in good agreement to FA and ICGA.

FA and ICGA are also capable of investigating circulation by dye-dilution method. Macroscopic blood flow dynamics, e.g. circulation time, will be investigated which is difficult for OCA. Instead of that, OCA are capable of measuring the local blood flow speed, not absolute value but relative value, that is hard for fluorescence angiographies.

There is an alternative en-face method to contrast only the retinal vessels from the OCT volume sets by utilizing the absorption of blood, which is referred to as the shadowgram [54]. It might be useful to create composite colored images of the macular region. The comparison between an OCA image of the retina and a shadowgram, composite images from each image and an OCA image of the choroid are shown in Fig. 4.10. A finer retinal vasculature can be observed in the shadowgram and the composite image than in the OCA image of the retina. On the other hand, a OCT intensity based choroidal vessel imaging requires significantly deep penetration to the choroid. The high-speed swept-source OCT in the 1 micron wavelength region has been performed the deeper penetration and the high contrast choroidal vessel imaging [87].

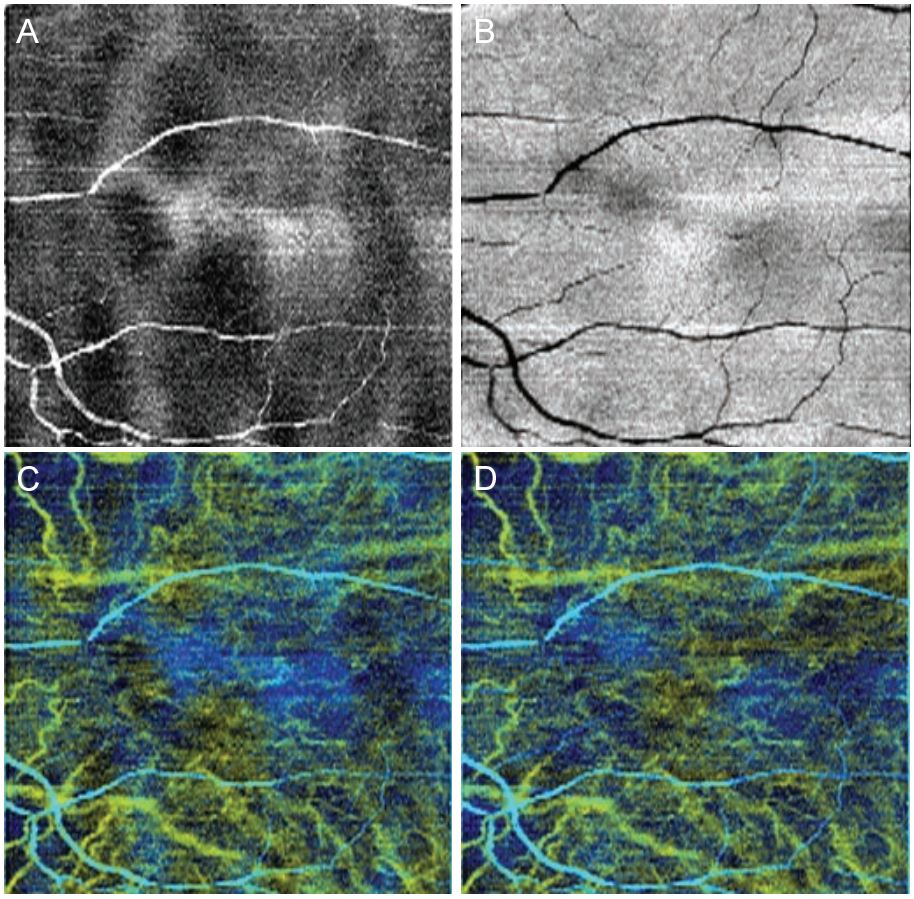

Figure 4.10: Composite image with shadowgram and flow projection image. As compared to the power of Doppler shift projection of the retinal part (A), the shadowgram (B) exhibits a fine retinal vasculature. The composite colored angiograms (C), (D) are obtained from the power of Doppler shift projection of the choroidal part (Fig. 4.6 (C)) and (A) or (B), respectively.

4.4 Summary

We present a new noninvasive angiography for the human eye. By using 3D flow imaging with high-speed SD-OCT, the 3D vasculature of the posterior part of the human eye is visualized. The retinal and choroidal parts are distinguished in the OCT images by segmentation. The two-dimensional vessel images of the retina and choroid represent the ocular vessels corresponding to FA and ICGA.

Chapter 5

Conclusion

The high-speed tissue imaging has been performed with SD-OCT. Although there are some difficulties, high-speed full-range complex SD-OCT has been performed. This technique will reduce the limitations of SD-OCT and extend its applicability.

As an application of SD-OCT, high-speed retinal imaging is performed for the *in vivo* human retina. The 3D observations of retinal diseases can not only lead to better diagnosis but also further our understanding of these diseases. The advanced application of SD-OCT, namely, OCA is also proposed. The three-dimensional blood flow maps for the retinal and choroidal vessels are obtained. The 3D information enables the production of multidimensional images such as false-colored *en-face* vessel images. OCA will be complementary to existing ophthalmic diagnosis tools and used as a hemodynamic investigation method.

Appendix A

Signal-to-noise ratio of SD-OCT

Consider that a single reflection surface is placed in the sample arm with a amplitude reflectivity, r_s, and an optical path length, z'. The axial profile of the sample is $a_s(z) = r_s\delta(z - z')$. The detected spectrum can be obtained by substituting this profile in eq. (1.1) as

$$I(k) = S(k)\left[R_r r_r^2 + R_s r_s^2 + 2\sqrt{R_r R_s} r_r r_s \cos(kz')\right]. \tag{A.1}$$

By photodetection at the linear detector array, a photon is converted into a charge. The number of generated charges is given by

$$\mathscr{N}(k_m) = \frac{\eta\tau}{h\nu_0} S(k_m)\left[R_r r_r^2 + R_s r_s^2 + 2\sqrt{R_r R_s} r_r r_s \cos(k_m z')\right]\Delta k, \tag{A.2}$$

where subscript m denotes the index of the detector ($m = 0, 1, 2, \cdots, N-1$) and Δk denotes wavenumber separation corresponding to the detector size. η denotes the quantum efficiency of the spectrometer including the diffraction efficiency and the quantum efficiency of the linear detector array; τ, the exposure time; h, Planck's constant; ν_0, the central optical frequency. The signal is the modulation in eq. (A.2) and is expressed as

$$\mathscr{N}_s(k_m) = 2\frac{\eta\tau}{h\nu_0} S(k_m)\sqrt{R_r R_s} r_r r_s \cos(k_m z')\Delta k. \tag{A.3}$$

The discrete Fourier transform (DFT) of the above equation yields the OCT signal $F_s(z_n)$ as,

$$\begin{aligned} F_s(z_n) &= \sum_{m=0}^{N-1} \mathscr{N}_s(k_m) \exp[-i2\pi mn/N] \\ &= \frac{\eta\tau}{h\nu_0}\sqrt{R_r R_s} r_r r_s P_0 V(z_n/c) \otimes \left[\delta(z_n - z') + \delta(z_n + z')\right]. \end{aligned} \tag{A.4}$$

The power of the light source $P_0 = \sum_{m=0}^{N-1} S(k_m)\Delta k$, assuming that the spectrometer covers the entire light source spectrum and the linear detector array has a fill

factor of 100%. The signal is concentrated at $z_n = \pm z'$. Considering only the positive path length difference region, the expected peak power of the signal is

$$\langle |F_s(z')|^2 \rangle = \left(\frac{\eta\tau}{h\nu_0} P_0 \right)^2 R_r R_s r_r^2 r_s^2. \tag{A.5}$$

The noise sources of SD-OCT are photon noise and detector noise. Photon noise is includes "shot noise" (which obeys Poisson distribution due to photon detection) and "excess photon noise" (caused by intensity fluctuations in the detected light) [88]. Broadband light sources such as a superluminescent diodes, are used in SD-OCT; therefore, the source used here can be assumed to be a partially polarized thermal source. The important factor in the excess photon noise statistics is the ratio of the integration time to the coherence time of light. Since SD-OCT resolves the spectrum, the coherence time of the portion, inverse of the effective optical bandwidth, is longer than that of the original emission. Although that, it is in the order of $\sim 10^{-11}$ s ($\sim$ 0.1 nm wavelength separation, ~ 1 μm central wavelength), which is much shorter than the integration time of high-speed SD-OCTs (~ 10 μs). Thus, the photon noise at each detector can be expressed as, [89],

$$\langle \mathscr{N}_{photon}^2(k_m) \rangle = \langle \mathscr{N}(k_m) \rangle \left[1 + \frac{1+\mathscr{P}^2}{2} \frac{2\pi}{c\Delta k \tau} \langle \mathscr{N}(k_m) \rangle \right], \tag{A.6}$$

where $\mathscr{P}$ denotes the degree of polarization; τ, the integration time; and c, the speed of light. $\mathscr{N}_{photon}$ denotes the photon noise equivalent number of the electron charge. The first term of eq. (A.6) correspoinds to the photon shot noise and the second term to the excess photon noise. After the Fourier transformation of $\mathscr{N}_{photon}$, the photon noise is expressed as,

$$\begin{aligned} \langle |F_{photon}(z_n)|^2 \rangle &= \left\langle \left| \sum_{m=0}^{N-1} \mathscr{N}_{photon}(k_m) e^{-j2\pi nm/N} \right|^2 \right\rangle \\ &= \sum_{m=0}^{N-1} \langle \mathscr{N}_{photon}^2(k_m) \rangle. \end{aligned} \tag{A.7}$$

Then, the photon shot noise becomes

$$\begin{aligned} \langle |F_{shot}(z_n)|^2 \rangle &= \sum_{m=0}^{N-1} \langle \mathscr{N}(k_m) \rangle \\ &= \frac{\eta\tau}{h\nu_0} P_0 (R_r r_r^2 + R_s r_s^2). \end{aligned} \tag{A.8}$$

Furthermore, the excess photon noise becomes

$$\begin{aligned} \langle |F_{excess}(z_n)|^2 \rangle &= \frac{1+\mathscr{P}^2}{2} \frac{2\pi}{c\Delta k \tau} \sum_{m=0}^{N-1} \langle \mathscr{N}(k_m) \rangle^2 \\ &= \frac{1+\mathscr{P}^2}{2\Delta\nu_{eff}\tau} \left[\frac{\eta\tau}{h\nu_0} P_0 (R_r r_r^2 + R_s r_s^2) \right]^2, \end{aligned} \tag{A.9}$$

where $\Delta\nu_{eff}$ is the bandwidth of the light source.

In addition, there are several noise sources in the detection part, namely, the dark noise of the detector, amplifier noise, and quantization noise at digitization. All these noises are together termed as the detection noise $\langle \mathscr{N}^2_{detect} \rangle$ for each detector of a linear sensor. When all these noises can be assumed as white noise, the detection noise in the time domain is given by

$$\langle |F_{detect}(z_n)|^2 \rangle = N \langle \mathscr{N}^2_{detect} \rangle. \tag{A.10}$$

Then, the signal-to-noise ratio of SD-OCT will is given by

$$SNR = \frac{\left(\frac{\eta\tau}{h\nu_0} P_0\right)^2 R_r R_s r_r^2 r_s^2}{\frac{\eta\tau}{h\nu_0} P_0 (R_r r_r^2 + R_s r_s^2) \left[1 + \frac{1+\mathscr{P}^2}{2\Delta\nu_{eff}\tau} \frac{\eta\tau}{h\nu_0} P_0 (R_r r_r^2 + R_s r_s^2)\right] + N \langle \mathscr{N}^2_{detect} \rangle}. \tag{A.11}$$

In OCTs, the backscattering coefficient of tissues is considered to be sufficiently smaller than the reference arm reflectivity; as a result, the photon noise contribution from the backscattered sample light can be ignored. Consequently, the SNR limited by each noise source can be expressed as

$$SNR_{shot} = \frac{\eta\tau}{h\nu_0} P_0 R_s r_s^2 \tag{A.12}$$

$$SNR_{excess} = \frac{2\Delta\nu_{eff}\tau}{1+\mathscr{P}^2} \frac{R_s r_s^2}{R_r r_r^2} \tag{A.13}$$

$$SNR_{detect} = \left(\frac{\eta\tau}{h\nu_0} P_0\right)^2 \frac{R_r R_s r_r^2 r_s^2}{N \langle \mathscr{N}^2_{detect} \rangle}. \tag{A.14}$$

Appendix B

Calibration of the spectrometer

In OCT systems, the depth information of tissues is encoded into time-of-flight of the backscattered light and decoded by means of time cross-correlation with the original light source. In the SD-OCT systems, this information is retrieved from its Fourier counterpart, i.e. the spectral-domain signal. The spectral fringes are detected by a high-speed spectrometer; however, the sampling is not evenly spaced in frequency, which is the Fourier counterpart of time. Thus, resampling is required to obtain spectral signals with a constant period in frequency.

To obtain the resampling points, the phase of the spectral interference signal is used. Since the phase of the interference signal is linear to the optical frequency when there is no chromatic dispersion, it provides correct resampling points. A single reflective surface, such as a mirror, is placed in the probing arm of the interferometer, and the spectral signal is obtained with the spectrometer. Then, the interferometric term can be expressed by using eq. (1.1) as

$$\tilde{I}[k(x_i)] = 2S[k(x_i)]\sqrt{R_r R_s} r_r r_s \cos\big[2k(x_i)z_0\big], \tag{B.1}$$

where r_s is the amplitude reflectivity of the reflective surface and x_i is the position of each pixel on a linear detector array. The phase of this fringe signal can be obtained by using the Hilbert transform or the Fourier transform method (FTM) [39]. Here, FTM is used to avoid unnecessary signals such as fixed-pattern noise and to increase the signal-to-noise ratio. The obtained complex interference signal is given by

$$\tilde{I}'[k(x_i)] = S[k(x_i)]\sqrt{R_r R_s} r_r r_s \exp[j\phi(x_i)], \tag{B.2}$$

where

$$\phi(x_i) = 2k(x_i)z_0 = 4\pi \frac{\nu(x_i)}{c} z_0. \tag{B.3}$$

Since $\phi \propto \nu$, the resampling point set x_l' has to sampled ϕ as a linear function. The inverse function of $\phi(x_i)$ is fitted by a polynomial; then it can be expanded as

$$x(\phi_i) = a_0 + a_1\phi_i + a_2\phi_i^2 + a_3\phi_i^3 + \cdots . \tag{B.4}$$

Thus, the resampling point set x'_l can be created by using an even-spaced phase set given by

$$x'_l = a_0 + a_1(\phi_0 + l\Delta\phi) + a_2(\phi_0 + l\Delta\phi)^2 + a_3(\phi_0 + l\Delta\phi)^3 + \cdots . \quad \text{(B.5)}$$

Third-order polynomial fitting is applied to the high-speed ophthalmic SD-OCT system (Sec. 3.1), and the fourth-order fitting to the UHR-SD-OCT system (Sec. 3.2). The calibrated spectral signals at these resampling points are obtained by linear interpolation after zero-padding [90]. The same method is also used in the swept-source OCT system [91].

The main feature of this method is the use of a phase of interferometric signal, which is proportional to frequency (eq. (B.3)). Thus, it is not feasible to use a single reflective surface in cases where a dispersion mismatch between the two arms of interferometer exists. In these cases, a common path configuration can be used, e.g., placing a glass plate and a mirror with narrow air gap in the same arm. There is no dispersion mismatch between the reflected light from the back surface of the glass and the mirror. Another method is to subtract the phases of two different interference signals with different optical path length differences z_0. In this case, the dispersion mismatch between two arms will be canceled out.

References

[1] D. Huang, E. A. Swanson, C. P. Lin, J. S. Schuman, W. G. Stinson, W. Chang, M. R. Hee, T. Flotte, K. Gregory, C. A. Puliafito, and J. G. Fujimoto, "Optical coherence tomography," Science **254**, 1178–1181 (1991).

[2] J. Schuman, C. Puliafito, and J. Fujimoto, *Optical Coherence Tomography of Ocular Diseases*, 2nd ed. (SLACK Inc., Thorofare, NJ, 2004).

[3] J. Welzel, "Optical coherence tomography in dermatology: a review." Skin Res. Technol. **7**(1), 1–9 (2001).

[4] B. E. Bouma, G. J. Tearney, C. C. Compton, and N. S. Nishioka, "High-resolution imaging of the human esophagus and stomach in vivo using optical coherence tomography." Gastrointest. Endosc. **51**(4 Pt 1), 467–474 (2000).

[5] I.-K. Jang, B. E. Bouma, D.-H. Kang, S.-J. Park, S.-W. Park, K.-B. Seung, K.-B. Choi, M. Shishkov, K. Schlendorf, E. Pomerantsev, S. L. Houser, H. T. Aretz, and G. J. Tearney, "Visualization of coronary atherosclerotic plaques in patients using optical coherence tomography: comparison with intravascular ultrasound." J. Am. Coll. Cardiol. **39**(4), 604–609 (2002).

[6] B. T. Amaechi, S. M. Higham, A. G. Podoleanu, J. A. Rogers, and D. A. Jackson, "Use of optical coherence tomography for assessment of dental caries: quantitative procedure." J. Oral Rehabil. **28**(12), 1092–1093 (2001).

[7] S. W. Jeon, M. A. Shure, K. B. Baker, D. Huang, A. M. Rollins, A. Chahlavi, and A. R. Rezai, "A feasibility study of optical coherence tomography for guiding deep brain probes." J. Neurosci. Methods **154**(1-2), 96–101 (2006).

[8] W. Drexler, U. Morgner, F. Kartner, C. Pitris, S. Boppart, X. Li, E. Ippen, and J. Fujimoto, "Invivo ultrahigh-resolution optical coherence tomography," Opt. Lett. **24**(17), 1221–1223 (1999). URL http://ol.osa.org/abstract.cfm?id=37426.

[9] A. Rollins, S. Yazdanfar, M. Kulkarni, R. Ung-Arunyawee, and J. Izatt, "In vivo video rate optical coherence tomography," Opt. Exp. **3**(6), 219–229 (1998). URL http://www.opticsexpress.org/abstract.cfm?id=63318.

[10] J. F. de Boer and T. E. Milner, "Review of polarization sensitive optical coherence tomography and Stokes vector determination," J. Biomed. Opt. **7**(3), 359–371 (2002).

[11] S. Jiao, W. Yu, G. Stoica, and L. V. Wang, "Contrast Mechanisms in Polarization-Sensitive Mueller-Matrix Optical Coherence Tomography and Application in Burn Imaging," Appl. Opt. **42**(25), 5191–5197 (2003). URL http://ao.osa.org/abstract.cfm?id=74128.

[12] Y. Zhao, Z. Chen, C. Saxer, S. Xiang, J. F. de Boer, and J. S. Nelson, "Phase-resolved optical coherence tomography and optical Doppler tomography for imaging blood flow in human skin with fast scanning speed and high velocity sensitivity," Opt. Lett. **25**(2), 114–116 (2000). URL http://ol.osa.org/abstract.cfm?id=291.

[13] Y. Zhao, Z. Chen, C. Saxer, Q. Shen, S. Xiang, J. F. de Boer, and J. S. Nelson, "Doppler standard deviation imaging for clinical monitoring of in vivo human skin blood flow," Opt. Lett. **25**(18), 1358–1360 (2000). URL http://ol.osa.org/abstract.cfm?id=62171.

[14] V. Westphal, S. Yazdanfar, A. M. Rollins, and J. A. Izatt, "Real-time, high velocity-resolution color Doppler optical coherence tomography," Opt. Lett. **27**(1), 34–36 (2002). URL http://ol.osa.org/abstract.cfm?id=67270.

[15] V. X. Yang, M. L. Gordon, B. Qi, J. Pekar, S. Lo, E. Seng-Yue, A. Mok, B. C. Wilson, and I. A. Vitkin, "High speed, wide velocity dynamic range Doppler optical coherence tomography(Part I): System design, signal processing, and performance," Opt. Exp. **11**(7), 794–809 (2003). URL http://www.opticsexpress.org/abstract.cfm?id=71869.

[16] D. Adler, T. Ko, P. Herz, and J. Fujimoto, "Optical coherence tomography contrast enhancement using spectroscopic analysis with spectral autocorrelation," Opt. Exp. **12**(22), 5487–5501 (2004). URL http://www.opticsexpress.org/abstract.cfm?id=81647.

[17] B. Hermann, K. Bizheva, A. Unterhuber, B. Považay, H. Sattmann, L. Schmetterer, A. Fercher, and W. Drexler, "Precision of extracting absorption profiles from weakly scattering media with spectroscopic time-domain optical coherence tomography," Opt. Exp. **12**(8), 1677–1688 (2004). URL http://www.opticsexpress.org/abstract.cfm?id=79601.

[18] C. Xu, D. Marks, M. Do, and S. Boppart, "Separation of absorption and scattering profiles in spectroscopic optical coherence tomography using a least-squares algorithm," Opt. Exp. **12**(20), 4790–4803 (2004). URL http://www.opticsexpress.org/abstract.cfm?id=81306.

[19] G. Häusler and M. W. Lindner, “”Coherence Radar” and ”Spectral Radar”–New Tools for Dermatological Diagnosis,” J. Biomed. Opt. **3**(1), 21–31 (1998).

[20] M. Wojtkowski, R. Leitgeb, A. Kowalczyk, T. Bajraszewski, and A. F. Fercher, “In vivo human retinal imaging by Fourier domain optical coherence tomography,” J. Biomed. Opt. **7**(3), 457–463 (2002).

[21] T. Mitsui, “Dynamic range of optical reflectometry with spectral interferometry,” Jpn. J. Appl. Phys. **38**, 6133–6137 (1999).

[22] R. Leitgeb, C. Hitzenberger, and A. Fercher, “Performance of fourier domain vs. time domain optical coherence tomography,” Opt. Exp. **11**(8), 889–894 (2003). URL http://www.opticsexpress.org/abstract.cfm?id=71990.

[23] J. F. de Boer, B. Cense, B. H. Park, M. C. Pierce, G. J. Tearney, and B. E. Bouma, “Improved signal-to-noise ratio in spectral-domain compared with time-domain optical coherence tomography,” Opt. Lett. **28**(21), 2067–2069 (2003). URL http://ol.osa.org/abstract.cfm?id=77739.

[24] N. Nassif, B. Cense, B. H. Park, S. H. Yun, T. C. Chen, B. E. Bouma, G. J. Tearney, and J. F. de Boer, “In vivo human retinal imaging by ultrahigh-speed spectral domain optical coherence tomography,” Opt. Lett. **29**(5), 480–482 (2004). URL http://ol.osa.org/abstract.cfm?id=78865.

[25] N. A. Nassif, B. Cense, B. H. Park, M. C. Pierce, S. H. Yun, B. E. Bouma, G. J. Tearney, T. C. Chen, and J. F. de Boer, “In vivo high-resolution video-rate spectral-domain optical coherence tomography of the human retina and optic nerve,” Opt. Exp. **12**(3), 367–376 (2004). URL http://www.opticsexpress.org/abstract.cfm?id=78765.

[26] T. Lindmo, D. J. Smithies, Z. Chen, J. S. Nelson, and T. E. Milner, “Accuracy and noise in optical Doppler tomography studied by Monte Carlo simulation.” Phys. Med. Biol. **43**(10), 3045–3064 (1998).

[27] B. E. Bouma and G. J. Tearney, eds., *Handbook of Optical Coherence Tomography* (Marcel Dekker, Inc., New York, 2002).

[28] P. Andretzky, M. W. Lindner, J. M. Herrmann, A. Schultz, M. Konzog, F. Kiesewetter, and G. Häusler, “Optical Coherence Tomography by spectral radar: dynamic range estimation and in vivo measurements of skin,” Proc. SPIE **3567**, 78–87 (1999).

[29] M. Choma, M. Sarunic, C. Yang, and J. Izatt, “Sensitivity advantage of swept source and Fourier domain optical coherence tomography,” Opt. Exp. **11**(18), 2183–2189 (2003). URL http://www.opticsexpress.org/abstract.cfm?id=78787.

[30] R. Leitgeb, W. Drexler, A. Unterhuber, B. Hermann, T. Bajraszewski, T. Le, A. Stingl, and A. Fercher, "Ultrahigh resolution Fourier domain optical coherence tomography," Opt. Exp. **12**(10), 2156–2165 (2004). URL http://www.opticsexpress.org/abstract.cfm?URI=OPEX-12-10-2156.

[31] A. Podoleanu and D. Jackson, "Noise Analysis of a Combined Optical Coherence Tomograph and a Confocal Scanning Ophthalmoscope," Appl. Opt. **38**(10), 2116–2127 (1999). URL http://ao.osa.org/abstract.cfm?id=44269.

[32] E. Swanson, D. Huang, M. Hee, J. Fujimoto, C. Lin, and C. Puliafito, "High-speed optical coherence domain reflectometry," Opt. Lett. **17**(2), 151–153 (1992). URL http://ol.osa.org/abstract.cfm?id=10980.

[33] S. Yun, G. Tearney, B. Bouma, B. Park, and J. de Boer, "High-speed spectral-domain optical coherence tomography at 1.3 μm wavelength," Opt. Exp. **11**(26), 3598–3604 (2003). URL http://www.opticsexpress.org/abstract.cfm?id=78225.

[34] M. Wojtkowski, A. Kowalczyk, R. Leitgeb, and A. Fercher, "Full range complex spectral optical coherence tomography technique in eye imaging," Opt. Lett. **27**(16), 1415–1417 (2002). URL http://ol.osa.org/abstract.cfm?id=69700.

[35] J. Greivenkamp and J. Bruning, *"Phase shifting interferometries," in Optical shop testing*, chap. 14, pp. 501–598, Wiley Series in Pure and Applied Optics, 2nd ed. (John Wiley & Sons Inc., New York, 1992).

[36] J. Schmit and K. Creath, "Extended averaging technique for derivation of error-compensating algorithms in phase-shifting interferometry," Appl. Opt. **34**(19), 3610–3619 (1995). URL http://ao.osa.org/abstract.cfm?id=46109.

[37] R. Leitgeb, C. Hitzenberger, A. Fercher, and T. Bajraszewski, "Phase-shifting algorithm to achieve high-speed long-depth-range probing by frequency-domain optical coherence tomography," Opt. Lett. **28**(22), 2201–2203 (2003). URL http://ol.osa.org/abstract.cfm?id=77783.

[38] E. Götzinger, M. Pircher, R. Leitgeb, and C. Hitzenberger, "High speed full range complex spectral domain optical coherence tomography," Opt. Exp. **13**(2), 583–594 (2005). URL http://www.opticsexpress.org/abstract.cfm?id=82398.

[39] M. Takeda, H. Ina, and S. Kobayashi, "Fourier-transform method of fringe-pattern analysis for computer-based topography and interferometry," J. Opt. Soc. Am **72**(1), 156–160 (1982). URL http://www.opticsinfobase.org/abstract.cfm?URI=josa-72-1-156.

[40] J. W. Goodman, *Introduction to Fourier optics*, 2nd ed. (McGraw-Hill, 1996).

[41] A. N. S. Institute", *American National Standard for Safe Use of Lasers: ANSI Z136.1* (Laser Institute of America, Orlando, Florida, 2000).

[42] W. Drexler, H. Sattmann, B. Hermann, T. H. Ko, M. Stur, A. Unterhuber, C. Scholda, O. Findl, M. Wirtitsch, J. G. Fujimoto, and A. F. Fercher, "Enhanced visualization of macular pathology with the use of ultrahigh-resolution optical coherence tomography." Arch. Ophthalmol. **121**(5), 695–706 (2003).

[43] T. H. Ko, J. G. Fujimoto, J. S. Schuman, L. A. Paunescu, A. M. Kowalevicz, I. Hartl, W. Drexler, G. Wollstein, H. Ishikawa, and J. S. Duker, "Comparison of ultrahigh- and standard-resolution optical coherence tomography for imaging macular pathology." Ophthalmology **112**(11), 1922 (2005).

[44] G. Wollstein, L. A. Paunescu, T. H. Ko, J. G. Fujimoto, A. Kowalevicz, I. Hartl, S. Beaton, H. Ishikawa, C. Mattox, O. Singh, J. Duker, W. Drexler, and J. S. Schuman, "Ultrahigh-resolution optical coherence tomography in glaucoma." Ophthalmology **112**(2), 229–237 (2005).

[45] M. Wojtkowski, V. Srinivasan, T. Ko, J. Fujimoto, A. Kowalczyk, and J. Duker, "Ultrahigh-resolution, high-speed, Fourier domain optical coherence tomography and methods for dispersion compensation," Opt. Exp. **12**(11), 2404–2422 (2004). URL http://www.opticsexpress.org/abstract.cfm?URI=OPEX-12-11-2404.

[46] B. Cense, N. Nassif, T. Chen, M. Pierce, S. Yun, B. Park, B. Bouma, G. Tearney, and J. de Boer, "Ultrahigh-resolution high-speed retinal imaging using spectral-domain optical coherence tomography," Opt. Exp. **12**(11), 2435–2447 (2004). URL http://www.opticsexpress.org/abstract.cfm?URI=OPEX-12-11-2435.

[47] G. J. Tearney, B. E. Bouma, and J. G. Fujimoto, "High-speed phase- and group-delay scanning with a grating-based phase control delay line," Opt. Lett. **22**(23), 1811–1813 (1997). URL http://ol.osa.org/abstract.cfm?id=36459.

[48] W. Drexler, U. Morgner, R. K. Ghanta, F. X. Kärtner, J. S. Schuman, and J. G. Fujimoto, "Ultrahigh-resolution ophthalmic optical coherence tomography." Nat. Med. **7**(4), 502–507 (2001).

[49] A. Fercher, C. Hitzenberger, M. Sticker, R. Zawadzki, B. Karamata, and T. Lasser, "Numerical dispersion compensation for Partial Coherence Interferometry and Optical Coherence Tomography," Opt. Exp. **9**(12), 610–615 (2001). URL http://www.opticsexpress.org/abstract.cfm?URI=OPEX-9-12-610.

[50] D. L. Marks, A. L. Oldenburg, J. J. Reynolds, and S. A. Boppart, "Digital algorithm for dispersion correction in optical coherence tomography for homogeneous and stratified media." Appl. Opt. **42**(2), 204–217 (2003). URL http://ao.osa.org/abstract.cfm?id=70980.

[51] D. L. Marks, A. L. Oldenburg, J. J. Reynolds, and S. A. Boppart, "Autofocus algorithm for dispersion correction in optical coherence tomography." Appl. Opt. **42**(16), 3038–3046 (2003). URL http://ao.osa.org/abstract.cfm?id=72461.

[52] L. Ferman, H. Collewijn, T. C. Jansen, and A. V. V. den Berg, "Human gaze stability in the horizontal, vertical and torsional direction during voluntary head movements, evaluated with a three-dimensional scleral induction coil technique." Vision Res. **27**(5), 811–828 (1987).

[53] D. A. Atchison and G. Smith, *Optics of the human eye* (Butterworth-Heinemann, Oxford, UK, 2000).

[54] S. Jiao, R. Knighton, X. Huang, G. Gregori, and C. A. Puliafito, "Simultaneous acquisition of sectional and fundus ophthalmic images with spectral-domain optical coherence tomography," Opt. Exp. **13**(2), 444–452 (2005). URL http://www.opticsexpress.org/abstract.cfm?id=82381.

[55] J. Flammer, S. Orgul, V. P. Costa, N. Orzalesi, G. K. Krieglstein, L. M. Serra, J.-P. Renard, and E. Stefánsson, "The impact of ocular blood flow in glaucoma," Prog. Retin. Eye Res. **21**, 359–393 (2002).

[56] V. Patel, S. Rassam, R. Newsom, J. Wiek, and E. Kohner, "Retinal blood flow in diabetic retinopathy." BMJ **305**(6855), 678–683 (1992).

[57] E. Friedman, "A hemodynamic model of the pathogenesis of age-related macular degeneration," Am. J. Ophthalmol. **124**, 677–682 (1997).

[58] J. D. Gass, *Stereoscopic atlas of macular diseases*, 4th ed. (Mosby, 1997).

[59] L. Yannuzzi, K. Rohrer, L. Tindel, R. Sobel, M. Costanza, W. Shields, and E. Zang, "Fluorescein angiography complication survey," Ophthalmology **93**, 611–617 (1986). URL http://www.ncbi.nlm.nih.gov/entrez/query.fcgi?cmd=Retrieve&db=PubMed&list_uids=3523356&dopt=Citation.

[60] M. Hope-Ross, L. Yannuzzi, E. Gragoudas, D. Guyer, J. Slakter, J. Sorenson, S. Krupsky, D. Orlock, and C. Puliafito, "Adverse reactions due to indocyanine green," Ophthalmology **101**, 529–533 (1994).

[61] G. T. Feke, A. Yoshida, and C. L. Schepens, "Laser based instruments for ocular blood flow assessment," J. Biomed. Opt. **3**, 415–422 (1998).

[62] G. T. Feke and C. E. Riva, "Laser Doppler measurements of blood velocity in human retinal vessels." J. Opt. Soc. Am. **68**(4), 526–531 (1978). URL http://www.opticsinfobase.org/abstract.cfm?id=56960.

[63] C. E. Riva, G. T. Feke, B. Eberli, and V. Benary, "Bidirectional LDV system for absolute measurement of blood speed in retinal vessels," Appl. Opt. **18**(13), 2301–2306 (1979). URL http://ao.osa.org/abstract.cfm?id=23187.

[64] C. E. Riva, S. Harino, B. Petrig, and R. Shonat, "Laser Doppler flowmetry in the optic nerve," Exp. Eye Res. **55**(3), 499–506 (1992).

[65] C. E. Riva, S. D. Cranstoun, J. E. Grunwald, and B. L. Petrig, "Choroidal blood flow in the foveal region of the human ocular fundus," Invest. Ophthalmol. Vis. Sci. **35**(13), 4273–4281 (1994).

[66] R. Bonner and R. Nossal, "Model for laser Doppler measurements of blood flow in tissue," Appl. Opt. **20**(12), 2097–2107 (1981). URL http://ao.osa.org/abstract.cfm?id=24957.

[67] G. Michelson, B. Schmauss, M. Langhans, J. Haraznv, and M. Groh, "Principle, validity, and reliability of scanning laser Doppler flowmetry," J. Glaucoma **5**, 99–105 (1996).

[68] G. Michelson and B. Schmauss, "Two dimensional mapping of the perfusion of the retina and optic nerve head." Br. J. Ophthalmol. **79**(12), 1126–1132 (1995). URL http://bjo.bmjjournals.com/cgi/content/abstract/79/12/1126.

[69] J. Briers and A. Fercher, "Retinal blood-flow visualization by means of laser speckle photography," Invest. Ophthalmol. Vis. Sci. **22**, 255–259 (1982).

[70] Y. Tamaki, M. Araie, E. Kawamoto, S. Eguchi, and H. Fujii, "Noncontact, two-dimensional measurement of retinal microcirculation using laser speckle phenomenon," Invest. Ophthalmol. Vis. Sci. **35**, 3825–3834 (1994).

[71] X. Wang, T. Milner, and J. Nelson, "Characterization of fluid flow velocity by optical Doppler tomography," Opt. Lett. **20**(11), 1337–1339 (1995). URL http://ol.osa.org/abstract.cfm?id=34444.

[72] Z. Ding, Y. Zhao, H. Ren, J. S. Nelson, and Z. Chen, "Real-time phase-resolved optical coherence tomography and optical Doppler tomography," Opt. Exp. **10**(5), 236–245 (2002). URL http://www.opticsexpress.org/abstract.cfm?id=68299.

[73] V. X. Yang, M. L. Gordon, E. Seng-Yue, S. Lo, B. Qi, J. Pekar, A. Mok, B. C. Wilson, and I. A. Vitkin, "High speed, wide velocity dynamic range Doppler optical coherence tomography(Part II): Imaging in vivo cardiac dynamics of

Xenopus laevis," Opt. Exp. **11**(14), 1650–1658 (2003). URL http://www.opticsexpress.org/abstract.cfm?id=73356.

[74] S. Yazdanfar, A. M. Rollins, and J. A. Izatt, "Imaging and velocimetry of the human retinal circulation with color Doppler optical coherence tomography," Opt. Lett. **25**(19), 1448–1450 (2000). URL http://ol.osa.org/abstract.cfm?id=62199.

[75] S. Yazdanfar, A. M. Rollins, and J. A. Izatt, "In vivo imaging of human retinal flow dynamics by color Doppler optical coherence tomography." Arch. Ophthalmol. **121**(2), 235–239 (2003). URL http://archopht.ama-assn.org/cgi/content/abstract/121/2/235.

[76] J. K. Barton, J. A. Izatt, M. Kulkarni, S. Yazdanfar, and A. Welch, "Three-dimensional reconstruction of blood vessels from in vivo color Doppler optical coherence tomography images," Dermatology **198**(4), 355–361 (1999).

[77] M. Wojtkowski, V. Srinivasan, J. G. Fujimoto, T. Ko, J. S. Schuman, A. Kowalczyk, and J. S. Duker, "Three-dimensional retinal imaging with high-speed ultrahigh-resolution optical coherence tomography." Ophthalmology **112**(10), 1734–1746 (2005).

[78] U. Schmidt-Erfurth, R. A. Leitgeb, S. Michels, B. Povazay, S. Sacu, B. Hermann, C. Ahlers, H. Sattmann, C. Scholda, A. F. Fercher, and W. Drexler, "Three-dimensional ultrahigh-resolution optical coherence tomography of macular diseases," Invest. Ophthalmol. Vis. Sci. **46**, 3393–3402 (2005).

[79] R. Leitgeb, L. Schmetterer, W. Drexler, A. Fercher, R. Zawadzki, and T. Bajraszewski, "Real-time assessment of retinal blood flow with ultrafast acquisition by color Doppler Fourier domain optical coherence tomography," Opt. Exp. **11**(23), 3116–3121 (2003). URL http://www.opticsexpress.org/abstract.cfm?id=77934.

[80] B. R. White, M. C. Pierce, N. Nassif, B. Cense, B. H. Park, G. J. Tearney, B. E. Bouma, T. C. Chen, and J. F. de Boer, "In vivo dynamic human retinal blood flow imaging using ultra-high-speed spectral domain optical Doppler tomography," Opt. Exp. **11**(25), 3490–3497 (2003). URL http://www.opticsexpress.org/abstract.cfm?id=78206.

[81] T. C. Chen, B. Cense, M. C. Pierce, N. Nassif, B. H. Park, S. H. Yun, B. R. White, B. E. Bouma, G. J. Tearney, and J. F. de Boer, "Spectral domain optical coherence tomography: ultra-high speed, ultra-high resolution ophthalmic imaging." Arch. Ophthalmol. **123**(12), 1715–1720 (2005).

[82] B. H. Park, M. C. Pierce, B. Cense, S.-H. Yun, M. Mujat, G. J. Tearney, B. E. Bouma, and J. F. de Boer, "Real-time fiber-based multi-functional spectral-domain optical coherence tomography at 1.3 μm," Opt. Exp. **13**(11), 3931–

3944 (2005). URL http://www.opticsexpress.org/abstract.cfm?id=84093.

[83] V. X. Yang, M. L. Gordon, A. Mok, Y. Zhao, Z. Chen, R. S. Cobbold, B. C. Wilson, and I. A. Vitkin, "Improved phase-resolved optical Doppler tomography using Kasai velocity estimator and histogram segmentation," Opt. Commun. **208**, 209–214 (2002).

[84] D. Freedman and P. Diaconis, "On the histogram as a density estimator: L2 theory," Probab. Theory Related Fields **57**, 453–476 (1981).

[85] D. W. Scott, *Multivariate Density Estimation: Theory, Practice, and Visualization* (John Wiley & Sons, Inc., New York, 1992).

[86] M. Mujat, R. C. Chan, B. Cense, B. H. Park, C. Joo, T. Akkin, T. C. Chen, and J. F. de Boer, "Retinal nerve fiber layer thickness map determined from optical coherence tomography images," Opt. Exp. **13**(23), 9480–10,216 (2005). URL http://www.opticsexpress.org/abstract.cfm?id=86235.

[87] E. C. Lee, J. F. de Boer, M. Mujat, H. Lim, and S. H. Yun, "In vivo optical frequency domain imaging of human retina and choroid," Opt. Exp. **14**(10), 4403–4411 (2006). URL http://oe.osa.org/abstract.cfm?id=89920.

[88] J. Goodman, *Statistical Optics*, chap. 9, pp. 465–527 (John Wiley & Sons, Inc., New York, 2000).

[89] C. Mehta, *"Theory of photoelectron counting," in Progress in Optics*, vol. VIII, chap. 8, pp. 373–440 (North-Holland Publishing Company, Amsterdam, 1970).

[90] C. Dorrer, N. Belabas, J. Likforman, and M. Joffre, "Spectral resolution and sampling issues in Fourier-transform spectral interferometry," J. Opt. Soc. Am. B **17**(10), 1795–1802 (2000). URL http://josab.osa.org/abstract.cfm?id=62013.

[91] Y. Yasuno, V. D. Madjarova, S. Makita, M. Akiba, A. Morosawa, C. Chong, T. Sakai, K.-P. Chan, M. Itoh, and T. Yatagai, "Three-dimensional and high-speed swept-source optical coherence tomography for in vivo investigation of human anterior eye segments," Opt. Exp. **13**(26), 10,652–10,664 (2005). URL http://www.opticsexpress.org/abstract.cfm?id=86669.